UCLouvain

École polytechnique de Louvain

Review and application of atmospheric turbulence profile models for satellite-ground optical links

Author: **Adrien NIKKHAH**
Supervisor: **Claude OESTGES**
Readers: **Florian QUATRESOOZ, Danielle VANHOENACKER-JANVIER**
Academic year 2022-2023
Master [120] in Electrical Engineering

Acknowledgments

This master thesis benefited from the help of many people that deserve to be thanked.

I would like to thank my supervisor, Prof. Claude Oestges for his feedbacks on my work and availability.

I would like to thank Florian Quatresooz for all the help he brought, insightful discussions and for all the resources he provided such as measurements and WRF simulations data that were extensively used in this work.

I would like to thank also Prof. Danielle Vanhoenacker-Janvier for reading this document and participate in assessing my work.

Finally, I would like to thank my family and friends who have supported and encouraged me all along, gave me feedback about my writing, etc...

Abstract

Atmospheric turbulence profile models aim at estimating the vertical profile of the refractive index structure constant C_n^2 which is a measure of the strength of the turbulence. Strong temperature gradients and wind shears are responsible for the stochastic nature of the refractive index field in the atmosphere, causing rapid fluctuations of the phase and amplitude of the optical wavefront propagating. Measurement campaigns are expensive and sometimes impractical, making estimation a cheaper and more convenient alternative. A large number of models exist in the literature on various levels of complexity, this master thesis investigates three models. Two of them rely on the statistical treatment of the turbulence according to Kolmogorov's theory while the third is an empirical model based of the correlation existing between potential temperature structure constant and the buoyancy and wind shear. The performances of the three models are assessed thanks to the T-REX measurement campaign which provided vertical profiles of standard atmospheric parameters such as temperature and wind speed as well as thermosonde measurements of the C_n^2.

Contents

Chapter 1

Introduction and objectives

Optical Turbulence is one of the main impairments affecting the propagation of optical waves through the atmosphere and can be briefly described as follows: turbulent mixing of the atmosphere associated with temperature fluctuations are responsible for fluctuations of the refractive index, resulting in fast amplitude and phase variations of the propagating wavefront. These amplitude variations are also known as *scintillation*.

This phenomenon is of great importance when considering astronomical observations as well as optical telecommunications and can be entirely characterized by the refractive index structure constant $C_n^2(h)$. This parameter represents the strength of the turbulence and varies with altitude, time of the day and seasons. Vertical profiles of the C_n^2 can be used by adaptive optics systems to counter turbulence-induced wavefront deformations of astronomical images [1] but also to define an accurate link budget of an optical telecommunication link.

To that end, $C_n^2(h)$ profiles can be either measured or estimated. This master thesis is about the latter. First, the theoretical background gathering the mathematical and phenomenological description of the optical turbulence is presented in chapter 2.

Then the state of the art in chapter 3 introduces some parameters of interest, coming from integrals of the C_n^2 profile (hence they are called *integrated parameters*), followed by a description of the main instruments used for the measurement of optical turbulence parameters. This chapter ends with the presentation of a representative set of models used for the $C_n^2(h)$ estimation.

Three statistical models are presented with an in-depth description in chapter 4 and their behaviour and individual performances are discussed in chapter 5.

The performances of the three models are then compared to each others in terms of multiple metrics in order to determine their relative strengths and weaknesses in chapter 6.

Finally, the three models are used to estimate seeing values at Redu (in Belgium) and compare them to the values measured in-situ with a DIMM in chapter 7.

Chapter 2

Theoretical background

In order to study the impact of scintillation on the wavefront one must solve the wave equation with one particular difficulty, i.e. the propagation medium is random owing to the stochastic nature of the refractive index in the atmosphere. Because of this stochastic nature of the propagation medium, a mathematical tool is first presented to characterize a random quantity such as the refractive index: the *structure function*.

Kolmogorov's turbulence theory relies on the concept of structure function to describe the behaviour of the longitudinal wind velocity within the inertial subrange. It has been later shown that the refractive index follows a similar law. At this point the refractive index structure constant, C_n^2, is presented as a measure of the strength of the turbulence. Afterward the conditions of apparition of optical turbulence are detailed and a criterion of atmospheric stability is presented.

Finally the random wave equation is established from Maxwell's equations and is then solved using *Rytov's transformation*. Once this is done the amplitude of the electric field can be retrieved and its variance directly linked to the C_n^2 through a volume integral under the assumption of a homogeneous random medium. This final result motivates the need of models of the C_n^2 in order to evaluate the variability of the amplitude level for example.

2.1 Structure function

Many random fields cannot be considered as stationary or homogeneous (which is the spatial equivalent of stationarity). However, certain fields like wind velocity, temperature or even refractive index are said to be *locally homogeneous* which means that the difference of the values taken at different positions is a homogeneous quantity over a wide range of distances, even though the field itself is not homogeneous (but the difference is)[2]. The description of such random fields is done most conveniently with a *structure function*. Some notations are worth being introduced before anything else :

Some notations

- $B_u(\mathbf{R}_1, \mathbf{R}_2)$: covariance function of the random field $u(\mathbf{R})$ between locations $\mathbf{R}_1$ and $\mathbf{R}_2$
- $D_u(\mathbf{R}_1, \mathbf{R}_2)$: structure function of the random field $u(\mathbf{R})$ between locations $\mathbf{R}_1$ and $\mathbf{R}_2$
- $\Phi_u(\kappa)$: power spectrum of the random field $u(\mathbf{R})$, i.e. the Fourier Transform of $B_u(\mathbf{R}_1, \mathbf{R}_2)$
- $\langle \cdots \rangle$: ensemble average

A random function of a vector spatial variable $\mathbf{R} = (x, y, z)$ and, possibly, time t is called a *random field*. To fully describe a random field necessitates the knowledge of its joint probability distributions of all orders which is, in practice, impossible. Only the lower-order statistical moments are usually available and therefore used.

A first important notion is that of a *homogeneous* medium: In general, statistical homogeneity of the random field implies that the mean value of the field is constant and that correlations between random fluctuations in the field from point to point are independent of the chosen observation points, depending only on their vector separation[3]. The theoretical treatment of spatial fluctuations of a random field in terms of covariance and power spectral density relies on the homogeneity assumption but many random fields like wind speed, temperature or even refractive index fluctuations do not fulfill this condition; they are considered to be *locally homogeneous* which is less restrictive. These quantities are characterised by the following general expression for a random field u :

$$u(\mathbf{R}) = m(\mathbf{R}) + u_1(\mathbf{R})[3] \tag{2.1}$$

where $m(\mathbf{R})$ is a *slowly* varying mean and $u_1(\mathbf{R})$ is a statistically homogeneous fluctuation with mean value $\langle u_1(\mathbf{R}) \rangle = 0 \ \forall \mathbf{R}$. Mathematically, a random field is said to be *locally homogeneous* if $\langle u(\mathbf{R} + \boldsymbol{\rho}) - u(\mathbf{R}) \rangle$ AND $\langle [u(\mathbf{R} + \boldsymbol{\rho}) - u(\mathbf{R})]^2 \rangle$ are independent of $\mathbf{R}$[3, 2] where $\boldsymbol{\rho}$ is the vector difference between the two measurement points.

Locally homogeneous random fields are not studied through covariance functions but rather another tool, the *structure function* which, in general, writes as follows (where $\mathbf{R} = \mathbf{R}_2 - \mathbf{R}_1$) :

$$\begin{aligned} D_u(\mathbf{R}_1, \mathbf{R}_2) &= \langle [u(\mathbf{R}_1) - u(\mathbf{R}_1 + \mathbf{R})]^2 \rangle \\ &\approx \langle [u_1(\mathbf{R}_1) - u_1(\mathbf{R}_1 + \mathbf{R})]^2 \rangle [3] \end{aligned} \tag{2.2}$$

where the second line comes from the fact that the mean is *slowly* varying and therefore the difference is roughly 0. In the following, the structure function of a random field u will be denoted by $D_u(\mathbf{R})$.

The structure function can also be expressed as an integral of the 3-D power spectrum $\Phi_u(\boldsymbol{\kappa})$[3] :

$$D_u(\mathbf{R}) = \iiint_{-\infty}^{\infty} \Phi_u(\boldsymbol{\kappa})(1 - \cos(\boldsymbol{\kappa} \cdot \mathbf{R}))\, d^3\kappa \tag{2.3}$$

where $\boldsymbol{\kappa}$ is the 3-D spatial wave vector.

Finally it is interesting to show that for a statistically *homogeneous* and isotropic random field u, the structure function and the covariance are related as :

$$D_u(\mathbf{R}) = 2[B_u(0) - B_u(\mathbf{R})][3,\ 2] \tag{2.4}$$

The structure function is one of the keys in analyzing locally homogeneous random fields like the refractive index. It is also one of the major tools used by Kolmogorov to establish his turbulence theory describing the behaviour of the refractive index within the inertial subrange. The power spectrum will be of great interest later when looking for expressions of the variance of the amplitude of the propagating wavefront through a random medium and multiple models of increasing complexity have been established, some will be presented in further sections.
Now that the concepts of local homogeneity and structure function have been introduced one can dive in Kolmogorov's turbulence theory that gives an expression of the refractive index structure function and traces its fluctuations back to temperature fluctuations.

2.2 Optical turbulence

2.2.1 Refractive index structure function

Kolmogorov showed (under the hypotheses of local homogeneity, isotropy and inertial subrange fully determined by kinematic viscosity and average dissipation range), by using dimensional analysis, that the longitudinal structure function of wind velocity in the inertial subrange satisfies the universal 2/3 power law[3, 4, 5] :

$$D_V(R) = C_V^2 R^{2/3} \qquad l_0 << R << L_0 \tag{2.5}$$

where R is the distance separating the two measurement points and C_V^2 is the wind velocity structure constant (in units of $m^{4/3}/s^2$), it is a measure of the total amount of energy in the turbulence. L_0 and l_0 are the outer and inner scales respectively of the turbulence, they are the boundaries of the inertial subrange within which Equation 2.5 is valid. Below the inertial subrange, energy is supposed to be dissipated by heat such that there are no eddies smaller than l_0 and eddies of size greater than L_0 are highly nonisotropic because the horizontal dimension is much larger than the vertical dimension, due to stratification, and no general description of the structure function can be predicted[3]. The passage from the energy input region ($L > L_0$) toward the energy dissipation one ($L < l_0$) is illustrated in Figure 2.1.
Historically, the fundamental ideas and characterization of turbulence were developed in terms of the velocity fluctuations. A similar dimensional analysis applied to any conservative passive scalar (or conservative passive *additive*, said of a parameter keeping its property when moved in the atmosphere) concludes with a 2/3 power law for the structure function[4], this is the case of the potential temperature and the refractive index. The potential temperature θ is the temperature of a parcel of air of temperature T at a level p which is moved at a pressure level of $1000hPa$, i.e. :

$$\theta = T\left(\frac{1000}{p}\right)^{\frac{\gamma-1}{\gamma}} \tag{2.6}$$

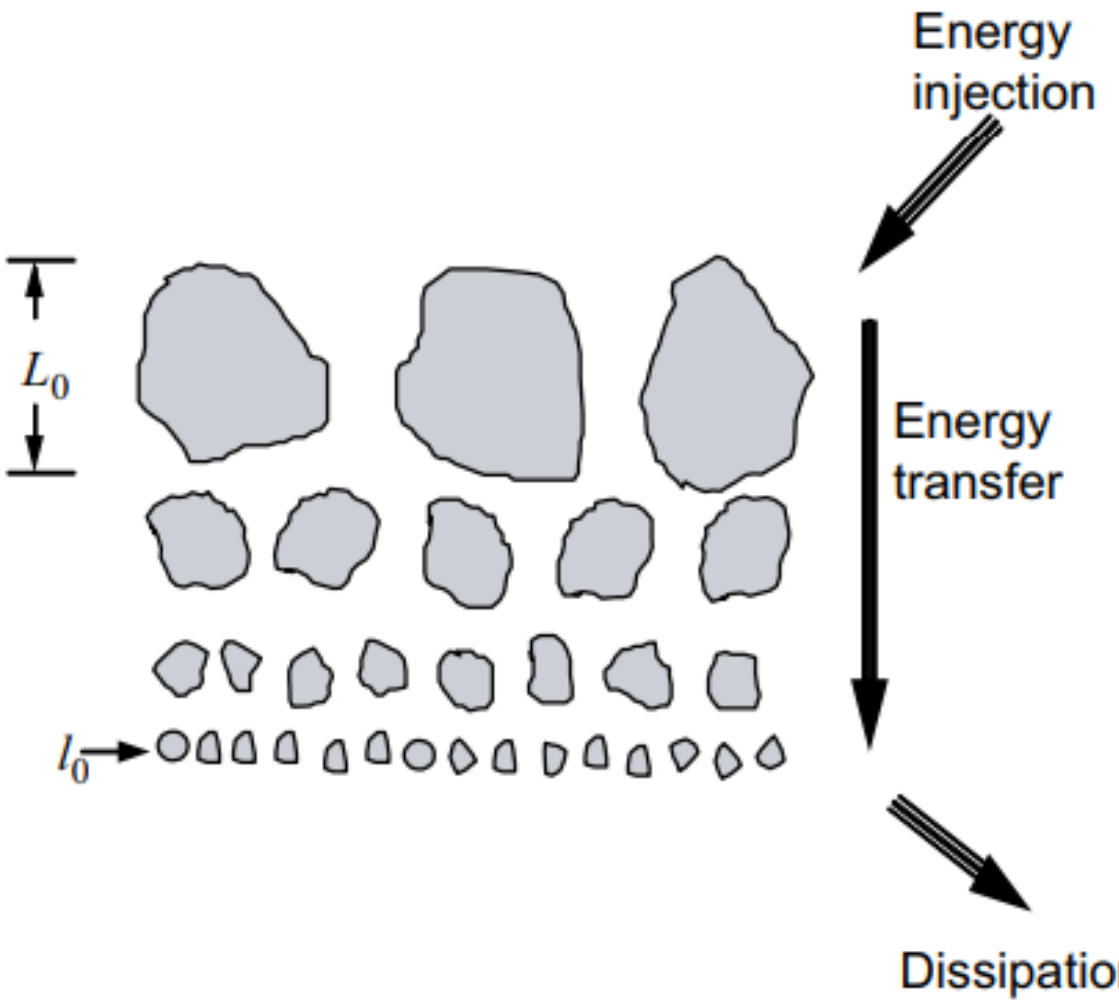

Figure 2.1: Kolmogorov cascade theory of turbulence, where L0 denotes the outer scale and l0 is the inner scale. Eddies between scale sizes l0 and L0 form the inertial subrange [3].

The refractive index n, one of the most significant parameters of the atmosphere for optical wave propagation, is very sensitive to small-scale temperature fluctuations. In particular, temperature fluctuations combined with turbulent mixing induce a random behavior in the field of atmospheric refractive index[3]. At a point $\mathbf{R}$ in space and time t, the refractive index can be expressed by :

$$n(\mathbf{R}, t) = n_0 + n_1(\mathbf{R}, t) \tag{2.7}$$

where $n_0 = \langle n(\mathbf{R}, t) \rangle \approx 1$ is the mean value of the refractive index and $n_1(\mathbf{R}, t)$ is the random deviation from the mean, with $\langle n_1(\mathbf{R}, t) \rangle = 0$. Supposing that the wave maintains a single frequency during the propagation, the time dependency from Equation 2.7 can be suppressed as follows :

$$n(\mathbf{R}) = 1 + n_1(\mathbf{R}) \tag{2.8}$$

This expression can be linked with Equation 2.1 that introduced the notion of local homogeneity which is one of the hypotheses used by Kolmogorov to develop his turbulence theory.

The statistical description of the random field of turbulence-induced fluctuations in the atmospheric refractive index is similar to that for the related random field of turbulent velocities. In particular, an inertial subrange exists bounded above by an outer scale L_0 and below by an inner scale l_0 . Also, when exhibited by the field of velocity fluctuations within the inertial subrange, the properties of statistical homogeneity and isotropy are inherited by the field of refractive-index fluctuations within the corresponding inertial subrange[3]. The refractive index structure function can therefore be expressed according to the 2/3 power law [4, 3, 5], i.e.:

$$D_n(R) = C_n^2 R^{2/3} \tag{2.9}$$

Furthermore, the structure constant C_n^2 of the refractive index n can be linked to the structure constant of potential temperature, as shown in [4], through Gladstone's formula:

$$C_n^2 = C_\theta^2 \left(\frac{Ap}{T^2}\right)^2 \tag{2.10}$$

where $A = 8 \cdot 10^{-5}$, p is the pressure and T is the temperature. The previous result of Equation 2.10 is very interesting because it is possible to measure the structure constant C_θ^2 with a balloon born equipment and from there, extract the C_n^2. This is one method of extracting an altitude profile of the refractive index structure constant however it is worth noting that it is rather tedious, suggesting that predicted (hence not measured) profiles would be interesting.

2.2.2 Stability criterion

This section presents a numerical criterion assessing the state of the atmosphere (turbulent or not), very similar to the Reynolds number in an isothermal fluid, i.e. the Richardson number R_i. It aims at summarizing some of the results in [4] and every equation and figure within this section originate from this reference.

The authors in [4] define the **two conditions** that must be fulfilled in order for the optical turbulence to appear :

- Dynamical turbulence
- Refractive index gradient

In an isothermal fluid, the stability criterion is given by the Reynolds number R_e, which is the ratio between the kinetic and viscosity energy. However, in a stratified fluid (as is the case for the atmosphere), the criterion of interest is the Richardson number R_i, giving the ratio between the potential and kinetic energy. This R_i governs the state, laminar or turbulent, of the atmosphere.

First, the static stability of the atmosphere can be evaluated thanks to the value of $\frac{d\theta}{dz}$ (where θ is the potential temperature and z the vertical coordinate) as shown in Figure 2.2. The static stability supposes no dynamical turbulence and hence no wind velocity gradient.

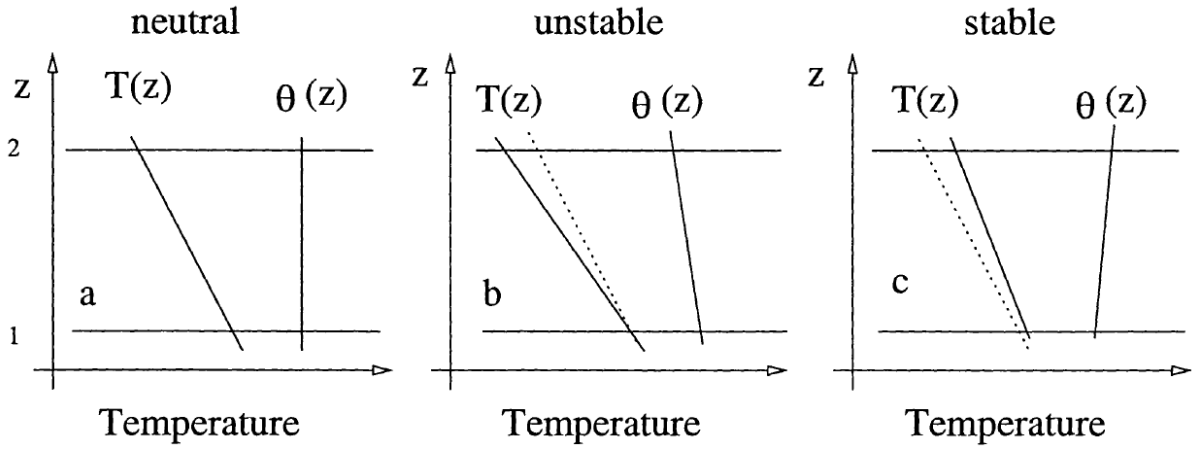

Figure 2.2: Three cases of static stability depending upon : (a) $\frac{d\theta}{dz} = 0$ neutral, (b) $\frac{d\theta}{dz} < 0$ unstable, (c) $\frac{d\theta}{dz} > 0$ stable. The dashed lines in (b) and (c) represent the adiabatic case [4].

- In situation (a) : a parcel of air moved from level 1 to level 2 will keep the same potential temperature and thus the same density as the air mass already present at level 2. Hence no buoyancy force is applied and the particle will stay at level 2 in a neutral stability.
- In situation (b) : a parcel raised at level 2 (along the dashed line) will be at a temperature higher than the rest of the other parcels and thus less dense. Hence the particle will tend to rise higher and higher, which is an unstable situation (convection).
- In situation 3 : a parcel raised adiabatically up to level 2 will be more dense than its environment and will therefore sink back to level 1. Similarly, a parcel lowered from level 1 will be less dense than the rest of the parcels and will rise back to level 1. In both cases, the particle moves toward its initial position, this is a stable situation.

But the gradient of potential temperature is not the only phenomenon able to generate instability. Indeed, wind also contributes and the dynamic stability must take this additional source into account. The expression of the Richardson number is the following :

$$R_i = \frac{E_p}{E_k} = \frac{g\Delta\rho\Delta z}{\rho\Delta U^2} \tag{2.11}$$

where the numerator is the potential energy per unit mass generated by a variation $\Delta\rho$ over vertical separation Δz and the denominator is the kinetic energy per unit mass generated by a wind shear ΔU [4]. Equation 2.11 can be rewritten in order to highlight the role of the potential temperature gradient $\frac{\Delta\theta}{\Delta z}$ and the wind velocity gradient $\frac{\Delta U}{\Delta z}$ and resumes to Equation 2.12. The intuition behind this ratio is that the potential temperature gradient is the key parameter as it is responsible for the refractive index gradient and also because an unstable $\frac{\Delta\theta}{\Delta z}$ creates a buoyancy force that will mix air parcels with different refractive index values. The wind velocity gradient tends to mix further those parcels but it can hardly create alone optical turbulence if there is no potential temperature gradient

already present.

$$R_i = \frac{\frac{g}{T}\frac{\Delta\theta}{\Delta z}}{(\frac{\Delta U}{\Delta z})^2} \tag{2.12}$$

Here again several cases can be analyzed:

- $R_i >> 0$ i.e. $\frac{\Delta\theta}{\Delta z} >> 0$, the temperature vertical stratification is very stable and the buoyancy forces impede the dynamical turbulence induced by the wind shear $\frac{\Delta U}{\Delta z}$.
- $R_i < 0$ the flow will be always turbulent since the potential temperature gradient is unstable.
- $0 < R_i < 1/4$ the flow is still turbulent even if the Richardson number is positive.

The three previous results are summarized in Figure 2.3 with an additional possible state which is the *fossil turbulence*.

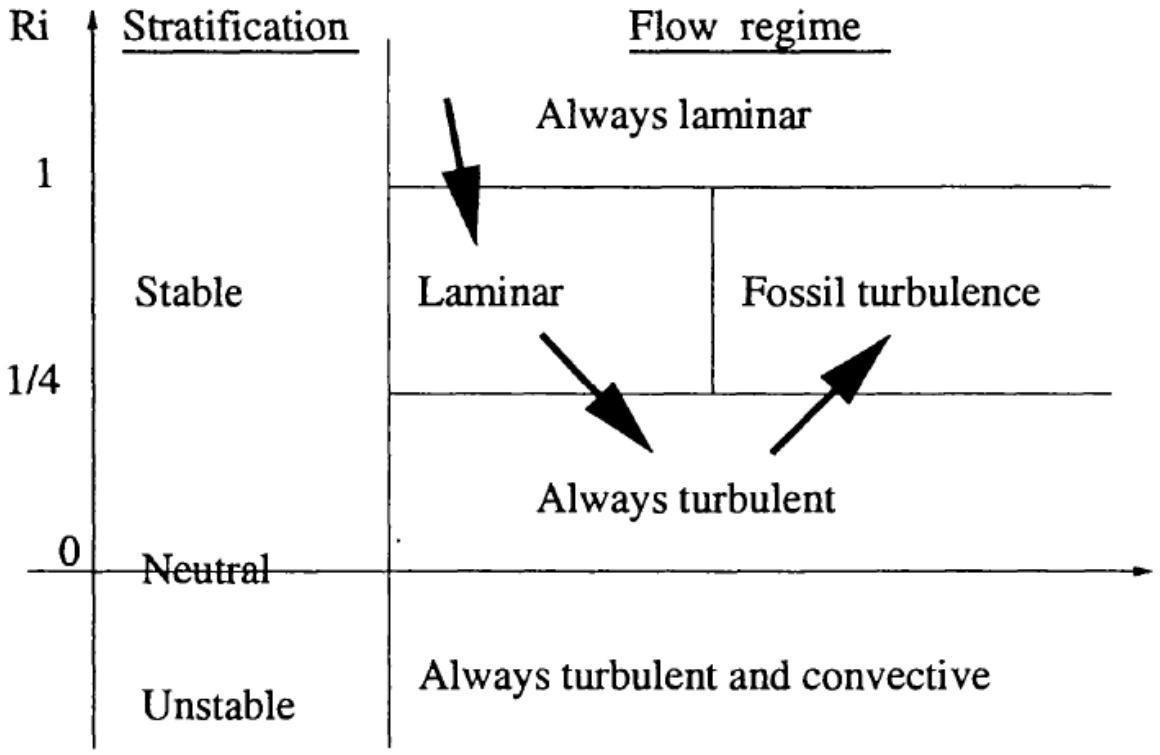

Figure 2.3: Various flow regimes depending on the Richardson number and its critical value 1/4. If positive, zero or negative the stratification is respectively stable, neutral or unstable (convective). If R_i is very large and positive, the flow is laminar, if it is negative the flow is convective and turbulent. Between 0 and 1/4 the flow is still turbulent and it can remain turbulent up to 1 for some time, this is the so-called *fossil turbulence* [4].

2.3 The random wave equation

After introducing some important notions like the structure function, Kolmogorov's turbulence theory and a phenomenological description of the origins of optical turbulence, it is

time to present the mathematical description of this phenomenon. The goal is to remind quickly Maxwell's equations and then present the wave equation in a random medium, without doing the development linking the two sets of equations.

The first step is to describe the propagation of an electromagnetic (EM) wave through a random medium. To do so one writes the Maxwell's equations (2.13 to 2.16)[5] linking the electric field (**E**), magnetic field (**H**), displacement field (**D**) and induction field (**B**) through the **curl** ($\nabla\times$) and **div** ($\nabla\cdot$) operators, **J** is the current density and ρ_e is the electric charge density.

$$\nabla \times \mathbf{E} = -\frac{1}{c}\frac{\partial \mathbf{B}}{\partial t} \tag{2.13}$$

$$\nabla \times \mathbf{H} = \frac{1}{c}\frac{\partial \mathbf{D}}{\partial t} + \frac{4\pi}{c}\mathbf{J} \tag{2.14}$$

$$\nabla \cdot \mathbf{D} = 4\pi\rho_e \tag{2.15}$$

$$\nabla \cdot \mathbf{B} = 0 \tag{2.16}$$

[5] uses Gaussian units for notational efficiency. Gaussian units are a set of units for electrical and magnetic quantities and usually simplifies the fundamental physical issues and theoretical relations involving electromagnetic phenomena[6]. They do not affect the results. In addition to the four Maxwell's equations, the constitutive equations describing the medium and introducing the permeability and permittivity, μ_m and ϵ respectively, must be added:

$$\mathbf{B} = \mu_m \mathbf{H} \tag{2.17}$$

$$\mathbf{D} = \epsilon(\mathbf{r}, t)\mathbf{E} \tag{2.18}$$

In this specific units system, $\mu_m = 1$ in earth's atmosphere such that **B** and **H** are virtually the same[5]. It is interesting here to note the relation $\epsilon = n^2$ linking the permittivity and refractive index. The equations will be expressed in terms of ϵ but the link with the refractive index is direct thanks to the previous relation. All the randomness of the medium is contained within the dielectric constant $\epsilon(\mathbf{r}, t)$. It is often decomposed into two parts, reminding again Equation 2.1:

$$\epsilon(\mathbf{r}, t) = \epsilon_0(\mathbf{r}) + \Delta\epsilon(\mathbf{r}, t) \tag{2.19}$$

The average $\epsilon_0(\mathbf{r})$ in the lower atmosphere differs from unity by less than $300ppm$ so from now on it is accepted that:

$$\epsilon(\mathbf{r}, t) = 1 + \Delta\epsilon(\mathbf{r}, t) \tag{2.20}$$

The fluctuating part $\Delta\epsilon(\mathbf{r}, t)$ is at the origin of the optical scintillation.
From this point, it is shown in [5] how to combine the previous relations to obtain a scalar wave equation that must be satisfied by each components of the **E** field being excited by the source, i.e. :

$$\nabla^2 E(\mathbf{r}) + k^2[1 + \Delta\epsilon(\mathbf{r}, t)]E(\mathbf{r}) = -4\pi i J(\mathbf{r}) \tag{2.21}$$

Equation 2.21 is the starting point to address the study of the impact of scintillation on the propagation of EM waves through the atmosphere. This equation has no exact analytical solution because $\Delta\epsilon(\mathbf{r}, t)$ is a stochastic function of time and position. However, some methods have been developed in order to find acceptable approximations. One of these methods is called *Rytov's transformation* and is presented next.

2.3.1 Rytov's transformation

The previous section established the *random wave equation* describing the propagation of an EM wave through a random medium, specifying that it has no exact solution. The aim of this section and the following is first to give an approximate solution using Rytov's transformation and then showing how the amplitude variance of the the electric field can be linked to the power spectrum of the permittivity under the assumption of a homogeneous random medium (an inhomogeneous random medium would use a different power spectrum, being now also a function of the mean position of the two points and not only the wave number vector $\boldsymbol{\kappa}$[5, 7]).

The Rytov approximation is fundamentally an enlargement of geometrical optics that includes diffraction effects. The essence of this method is to express the field strength as the product of the unperturbed field and the exponential of a surrogate function, which must be determined. It is a complex function that describes the important influence of diffraction because it is derived from the random-wave equation.[7]. This method allows to describe weak fluctuations in amplitude and intensity for both microwaves and optical propagation.

The fundamental problem in solving Equation 2.21 is that the random function $\delta\epsilon(\mathbf{r}, t)$ multiplies the function of interest itself i.e. E. *Rytov's transformation* achieves to separate these two functions, making $\delta\epsilon(\mathbf{r}, t)$ appear as an additional source term. The transformation is the following :

$$\mathbf{E}(\mathbf{r}) = \mathbf{E}_0(\mathbf{r})e^{\Psi(\mathbf{r})} \tag{2.22}$$

where $\mathbf{E}_0$ is the coherent field strength that would be measured in the absence of irregularities and $\Psi(\mathbf{r})$ is the surrogate function to determine. The random wave equation is then solved by expending the surrogate function as follows :

$$\Psi = \psi_1 + \psi_2 + \psi_3 + \cdots \tag{2.23}$$

The ψ_n is proportional to the n-th power of $\delta\epsilon$. The n-th order solution corresponds to a surrogate function made of the n first ψ_n. The basic Rytov solution (of order 1) is sufficient in a vast majority of applications but some may need higher order terms. Only the basic solution will be shown here. Following the development in [7], one gets an expression for the electric field :

$$\mathbf{E}_1(\mathbf{r}) = \mathbf{E}_0(\mathbf{r}) \exp\left(-k^2 \int G(\mathbf{R},\mathbf{r})\delta\epsilon(\mathbf{r}, t)\frac{\mathbf{E}_0(\mathbf{r})}{\mathbf{E}_0(\mathbf{R})}d^3r\right) \tag{2.24}$$

where G is the Green function. The Green function $G(x, s)$ is such that:

$$u(x) = \int G(x, s)f(s)ds$$

is a solution of

$$Lu(x) = f(x)$$

where L is a linear differential operator[8].

2.3.2 Amplitude variance

The signal amplitude is related logarithmically to the scattering integral as follows:

$$A(\mathbf{R}) = |\mathbf{E}_0(\mathbf{R})| \exp\left(-k^2 \int \mathbb{R}\left(G(\mathbf{R},\mathbf{r})\frac{\mathbf{E}_0(\mathbf{r})}{\mathbf{E}_0(\mathbf{R})}\right)\delta\epsilon(\mathbf{r},t)d^3r\right) \quad [7] \tag{2.25}$$

It leads naturally to the log-normal distribution of the fluctuations in amplitude and intensity. A more convenient representation is the logarithmic amplitude:

$$\chi = \log\left(\frac{A}{\mathbf{E}_0}\right) = -k^2 \int \mathbb{R}\left(G(\mathbf{R},\mathbf{r})\frac{\mathbf{E}_0(\mathbf{r})}{\mathbf{E}_0(\mathbf{R})}\right)\delta\epsilon(\mathbf{r},t)d^3r \quad [7] \tag{2.26}$$

The previous Equation 2.26 is a rather tedious expression to carry on so the following substitution is done, simply to ease the notations :

$$G(\mathbf{R},\mathbf{r})\frac{\mathbf{E}_0(\mathbf{r})}{\mathbf{E}_0(\mathbf{R})} = A(\mathbf{R},\mathbf{r}) + jB(\mathbf{R},\mathbf{r}) \quad [7] \tag{2.27}$$

be careful that $A(\mathbf{R},\mathbf{r}) \neq A(\mathbf{R})$ where the right term is the amplitude of the electric field. With this new notation the log amplitude can be re-written:

$$\chi = -k^2 \int A(\mathbf{R},\mathbf{r})\delta\epsilon(\mathbf{r},t)d^3r \quad [7] \tag{2.28}$$

and its first two statistical moments are as follows[7]:

$$\langle\chi\rangle = 0 \tag{2.29}$$

$$\langle\chi^2\rangle = k^4 \iint A(\mathbf{R},\mathbf{r})A(\mathbf{R},\mathbf{r'})\langle\delta\epsilon(\mathbf{r},t)\delta\epsilon(\mathbf{r'},t)\rangle d^3r d^3r' \tag{2.30}$$

where the mean log amplitude is zero because of the definition of $\delta\epsilon(\mathbf{r},t)$. The variance of the log amplitude is a very important quantity because it is directly linked to the transmit power of an optical communication system for example.
The spatial correlation in Equation 2.30 couples the two volume integrals in a complicated way and the expression can no longer be simplified without any further hypotheses about the propagation medium.

In the case of a homogeneous random medium, the analytical problem is simplified dramatically. One can here introduce the spectral representation of the spatial correlation as follows[7]:

$$\langle\delta\epsilon(\mathbf{r},t)\delta\epsilon(\mathbf{r'},t)\rangle = \int \Phi_\epsilon(\boldsymbol{\kappa})\exp(j\boldsymbol{\kappa}\cdot(\mathbf{r}-\mathbf{r'}))d^3\kappa \tag{2.31}$$

where $\Phi_\epsilon(\boldsymbol{\kappa})$ is the power spectrum of $\delta\epsilon$. Defining the *amplitude weighting function* (which must not be mistaken with a structure function, also designated by D) as:

$$D(\boldsymbol{\kappa}) = k^2 \int A(\mathbf{R},\mathbf{r})\exp(j\boldsymbol{\kappa}\mathbf{r})d^3\kappa \quad [7] \tag{2.32}$$

Equation 2.30 can be rewritten in a more compact form :

$$\langle \chi^2 \rangle = \int \Phi_\epsilon(\boldsymbol{\kappa}) D(\boldsymbol{\kappa}) D(-\boldsymbol{\kappa}) d^3\kappa \quad [7] \tag{2.33}$$

where the contribution of optical turbulence is concentrated in the power spectrum. At this point it is important to remind that $\epsilon = n^2$ such that their variations are linearly related, i.e. $\delta\epsilon(\mathbf{r}, t) \approx 2\delta n(\mathbf{r}, t)$[5] so their power spectrums also are linearly related.

Multiple power spectrum models have been developed in the literature such as Tatarskii's, von Karman's or the exponential spectrums. The simplest certainly is the Kolmogorov spectrum which is based on the 2/3 power law of the inertial subrange for the structure function of the refractive index and is the following[5, 3]:

$$\Phi_n(\boldsymbol{\kappa}) = 0.033 C_n^2 \boldsymbol{\kappa}^{11/3}, \quad \frac{1}{L_0} << \kappa << \frac{1}{l_0} \tag{2.34}$$

By plugging Equation 2.34 into Equation 2.33 it is clear that the variations of amplitude of the propagating wave are related to the C_n^2 through a volume integral.

This chapter layed down briefly the theoretical environment in which the optical turbulence has been defined and studied. The structure function and the corresponding power spectrum are given under the assumptions of a locally homogeneous and isotropic medium, introducing the key parameter of this master thesis i.e. the C_n^2. It has been shown that two conditions must be fulfilled in order for the optical turbulence to take place; there must be a refractive index gradient and dynamical turbulence must also be present. Furthermore, Rytov's transformation is presented as a method to find approximate solutions of the random wave equation Equation 2.21. Finally an expression of the variance of the log amplitude of the electric field is given and further developed in the case of a homogeneous random medium, highlighting the impact of the C_n^2 through the power spectrum (Equation 2.33). This chapter has proven the importance of the C_n^2 and as mentioned already, this parameter is not easily measured so the natural solution is to find accurate altitude models of the refractive index structure constant, relying on largely available meteorological data. This will be the subject of the next parts of this work.

Chapter 3

State of the art

Now that the mathematical tools as well as the conditions of apparition of optical turbulence have been presented, it is interesting to present the main parameters resulting from a given $C_n^2(h)$ vertical profile i.e. the integrated parameters. Then of course the principal measurement instruments relative to this phenomenon will be introduced and discussed briefly according to their working principle and specificities. Finally a representative set of estimation models, divided into three categories, are presented. This will provide the state of the art in the matter of scintillation.

3.1 Integrated parameters

Multiple parameters can be obtained from integrals of the vertical C_n^2 profile and they are of great interest when considering astronomy or optical telecommunications [9]. Such parameters are Fried's coherence length r_0, the isoplanatic angle θ_0 and the coherence time τ_0. They are of primary importance in the development of adaptive optics (AO) systems which is a technique aiming at correcting in real-time the turbulence-induced wavefront deformation of astronomical images taken from a ground-based telescope [1]. To do so it uses a wavefront sensor, corrector and an array of deformable mirrors to compensate the phase fluctuations [10]. AO have proved to be an efficient way to improve SNR with reduced transmit power [10].

3.1.1 Fried's parameter r_0

Fried's parameter is the spatial coherence length of the wavefront and represents the telescope diameter that would reach the same resolution if the observation conditions were ideal. It should be as large as possible [11] and is expressed as :

$$r_0 = \left(0.423k^2 \sec(\xi) \int_{h_0}^{\infty} C_n^2(h)dh\right)^{-3/5} \text{[1]} \tag{3.1}$$

where ξ is the zenith angle, h_0 is the ground altitude and $k = \frac{2\pi}{\lambda}$ is the wave number. As will be seen later, $C_n^2(h)$ is globally a decreasing function of the altitude such that the upper limit of the integral can be safely set to a finite value. In fact the decreasing

behaviour of $C_n^2(h)$ means that r_0 is mostly determined by the low-altitude values of the refractive index structure constant. Finally, from Equation 3.1 it appears that r_0 is a function of $\lambda^{6/5}$ and a value of the coherence length is therefore meaningful only when associated with a given wavelength.

Another frequently used parameter is the *seeing* ϵ_0. It is a major limitation of the angular resolution of an astronomical observation made by a telescope [12] and leads to the blurring of the received signal [10]. It is also the value of the full width at half maximum and represents the maximum resolution that can be achieved at a given time and site for a long exposure [11]. With ideal atmospheric conditions, the resolution is limited by the diffraction limit but taking into account optical turbulence, the effective telescope aperture diameter is replaced by r_0. The seeing is linked to the coherence length by the following expression :

$$\epsilon_0 = 0.98\frac{\lambda}{r_0}[11] \tag{3.2}$$

3.1.2 Isoplanatic angle θ_0

The isoplanatic angle θ_0 is the maximum angle within which the impairments due to optical turbulence are essentially identical [11, 1, 13]. It determines the area over which the wavefront corrected by an AO system is effective [13] such that θ_0 should also be as large as possible. Its expression as a function of the refractive index structure constant is the following :

$$\theta_0 = \left(2.91k^2 \sec^{8/3}(\xi) \int_{h_0}^{\infty} C_n^2(h) h^{5/3} dh\right)^{-3/5} [1] \tag{3.3}$$

Due to the presence of the weighing function $h^{5/3}$ in the integral of Equation 3.3, the isoplanatic angle is more sensitive to the high altitude layers of the C_n^2 than those near the ground, unlike the coherence length.

3.1.3 Coherence time τ_0

The coherence time τ_0 represents the temporal coherence of the wavefront and is also very important when studying AO systems since it gives the timescale on which the correction must operate [11, 13]. It is strongly dependant on the wind speed because the evolution of turbulent eddies usually operates on larger timescales than the time it takes for the wind to move an eddy from its own size [13] and it is the reciprocal of the Greenwood frequency f_G [12]. Its expression is the following :

$$f_G = 0.255 \left(k^2 \sec(\xi) \int_{h_0}^{\infty} C_n^2(h) V(h)^{5/3} dh\right)^{3/5} [1] \tag{3.4}$$

where $V(h)$ is the windspeed profile and

$$\tau_0 = \frac{1}{f_G}$$

Those three integrated parameters are illustrated in Figure 3.1.

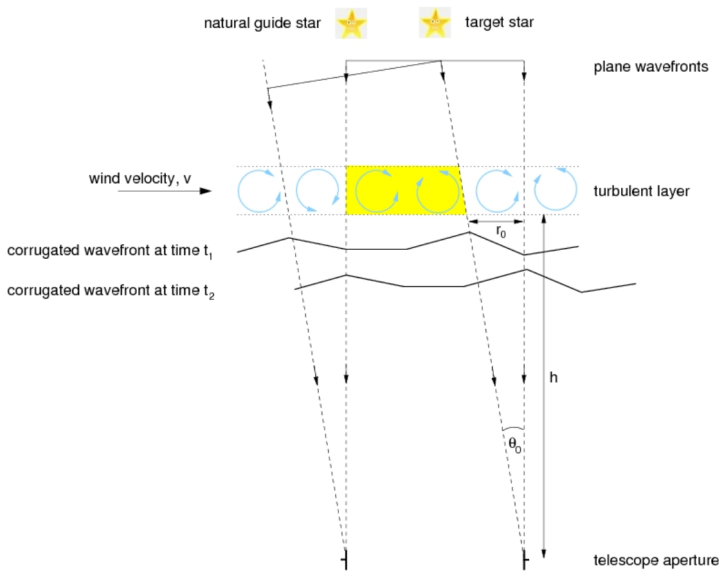

Figure 3.1: Schematic showing how r_0, θ_0 and τ_0 are defined [13].

3.2 Measurement instruments

There is a wide variety of instruments that have been developed in order to measure optical turbulence parameters, whether it is the full vertical $C_n^2(h)$ profile or some integrated parameters such as the seeing ϵ_0. This section presents some of the most used devices and their main working principles.

3.2.1 Thermosonde

Most information of this section comes from [14]. This instrument measures with high precision atmospheric parameters such as the windspeed, relative humidity, temperature, pressure and the potential temperature structure constant C_θ^2, all as a function of the altitude h. The knowledge of all these parameters in addition with Gladstone formula Equation 2.10 allows to retrieve the vertical profile of the refractive index structure constant C_n^2. The determination of C_θ^2 is the key element to this method and relies on the assumption that potential temperature is a passive conservative scalar following Kolmogorov theory of turbulence, meaning that its structure function within the inertial range ($l_0 << r << L_0$) follows the 2/3 power law :

$$D_\theta(r) = C_\theta^2 r^{2/3} \tag{3.5}$$

The structure function $D_\theta(r)$ is measured with two temperature probes spaced of a known distance r and the structure constant is then retrieved. The first flights of thermosonde-equipped balloons go back to the 1970's with Bufton et al. and, even though some improvements have been made, the principle remains the same. This method presents the finest vertical resolution among all others (around $1m$ to $10m$).

The cost of one equipped balloon is around 1000 USD (according to the authors in 2005) such that this technique is expected to be used for astronomical site testing when no other

technique could be used or if a high vertical resolution is needed. In addition to the high cost, the launch process is long and requires a consequent work force, limiting the number of launches to about 4 per night, resulting in a very poor temporal resolution [11].

3.2.2 SCIDAR

SCIntillation Detection And Ranging (SCIDAR) is an instrument developed by Azouit and Vernin (1980) to extract turbulence-related parameters such as the $C_n^2(h)$ and $V(h)$ vertical profiles from spatio-temporal correlations of an image of a double star. It is able to produce a vertical C_n^2 profile from $2km$ up to the stratosphere every $10s$ with a vertical resolution of $2.3km$. This vertical resolution depends on the angular separation of the double star and could be improved [15, 1]. Some later versions of the SCIDAR even managed to provide measurements of the near ground turbulence [1]. This is the first ground-based instrument able to measure the vertical structure of the turbulent layers as well as their characteristics. However, it needs a human intervention to monitor the measurements [11].

3.2.3 DIMM

The Differential Image Motion Monitor (DIMM) developed by Sarazin and Roddier (1990) is an instrument used to measure the seeing ϵ_0. Its main advantage compared to previous image motion monitors (such as the absolute image motion monitor) is that it is inherently insensitive to tracking errors [16]. It relies on analytical developments from Kolmogorov's theory to retrieve the seeing from directly measurable parameters [16]. It does not provide information on any other parameters such as the wind or C_n^2 profiles. It has a very good temporal resolution (one ϵ_0 estimate per minute) and operates autonomously (even though human intervention might be needed) [16, 11].

3.2.4 MASS

The Multi-Aperture Scintillation Sensor (MASS) consists in 4 concentric annular apertures yielding the C_n^2 for 6 different layers (depending on geometrical aspects) : $0.5km$, $1km$, $2km$, $4km$, $8km$ and $16km$ [11]. It retrieves the integral of the refractive index structure constant by measuring the differential relative intensity fluctuations, calculated as the variance of the natural logarithm of the intensity ratio of I_1 and I_2. I_1 is the intensity of light in the inner zone and I_2 is the intensity of light in the outer annular zone [17]. This instrument is not able to sense the the seeing in the lower parts of the atmosphere but can be coupled to other devices to do so [17, 11], it is the case e.g. of the DIMM-MASS used for seeing measurements at the Maunakea observatory [18].

The different instruments presented in this section all have advantages but also present some drawbacks as being expensive, needing a large work force for deployment or having a poor spatial or temporal resolution. Furthermore, it is sometimes difficult or even impractical to deploy such equipment in a given place [19]. Those arguments motivate the utility of models able to provide estimations of the optical turbulence-related parameters and more precisely, of the refractive index structure constant vertical profile $C_n^2(h)$.

3.3 Models

Estimation is a cheaper alternative to measurement campaigns since it does not require any material nor work force to deploy it. Therefore an accurate model would represent a valuable tool in assessing a potential astronomical site or as input to an AO system or even for designing the link budget of satellite/ground optical communication systems.

There is a wide variety of models estimating the vertical profile of the refractive index structure constant C_n^2, some based on physical equations, on statistical treatment of turbulence or simply on a database of measured profiles. This section aims at introducing a representative number of such models, classified in three different categories, according to their inputs and solving strategies.

The three categories are : static models, statistical models and numerical models. They are ranked in increasing order of complexity and performance. The second category of models (statistical) will be discussed here as well as in the following chapters. Because they offer a good trade-off between complexity and performance, they will be the subject of a more in-depth study and discussion.

3.3.1 Static models

Static models were obtained as a fitting for the mean measured $C_n^2(h)$ profile from a given measurement campaign. They do not rely on any (or very little) physical concept and do not give any physical insight on the phenomenon itself, i.e. optical turbulence. They are highly site dependent and a model developed according to a database from one site used at another location will most likely produce results far from the reality. Furthermore, $C_n^2(h)$ profiles vary strongly from night to day conditions such that a model is often designed for one of the two cases rather than both. Finally, instead of capturing all of the vertical fluctuations of the C_n^2, they provide a smooth and generalized trendline [20]. However, these models are extremely easy to use and only need a very few number of input parameters : mainly the height h above mean sea level and sometimes an rms wind speed value at a certain altitude and a ground value of C_n^2.

Hufnagel-Valley

The Hufnagel-Valley model was first developed according to scintillation and thermosonde measurements and in an attempt to correlate the scintillation spectrum with wind parameters [20]. It effectively represents the stratified structure of the refractive index structure constant as a sum of multiple exponential terms [21]. The model is expressed as follows :

$$C_n^2(h) = C_n^2(h_0)\exp(-10h) + A\exp(\frac{-h}{1.5}) + Bv^2h^{10}\exp(-h)[21] \tag{3.6}$$

where $C_n^2(h_0)$ is the value of C_n^2 at a reference ground altitude, v is the rms wind speed between 5 and $20km$ altitude, $A = 2.7 * 10^{-16}$ and $B = 8.148 * 10^{-26}$. Additional terms can be added to Equation 3.6 in order to represent additional turbulent layers as in [1]. The default values for v and $C_n^2(h_0)$ are $21m/s$ and $1.7 * 10^{-14}m^{-2/3}$ respectively [21] and the resulting model is known as the $HV_{5/7}$ because it corresponds to a $r_0 = 5cm$ and

$\theta_0 = 7\mu rad$. The Hufnagel-Valley model is the most widely used [10] and has also been often modified to adapt either to the location of a new site or for a night time use, etc... The main improvement was about the boundary layer and resulted in the HAP model [21, 22].

The Hufnagel-Valley model and its derivatives are easy-to-use and allow some freedom in modeling the high and low altitude values through the parameters v^2 and $C_n^2(h_0)$. They are valid throughout the whole atmosphere and are most suited for mid-latitude locations [22].

CLEAR 1

Most information of this section comes from [20]. Critical Laser Enhancing Atmospheric Research (CLEAR) is a model that has been developed on the same basis as Hufnagel-Valley (HV), i.e. scintillation (30 consecutive nights) and thermosonde (18 flights) measurements in New Mexico during summer 1984. The authors have divided the atmosphere in 4 different layers, ranging from ground up to $30km$ and each layer is characterized by an analytical expression for the C_n^2 profile. The mathematical expression is the following :

$$\log(C_n^2(h)) = \begin{cases} 0 & \text{if } h < 1.23km \\ -10.7025 - 4.3507h + 0.8141h^2 & \text{if } 1.23 < h < 2.13km \\ -16.2897 + 0.0335h - 0.0134h^2 & \text{if } 2.13 < h < 10.34km \\ -17.0577 - 0.0499h - 0.0005h^2 + 0.6181e^{-5\left(\frac{h-15.5617}{3.466}\right)^2} & \text{if } 10.34 < h < 30km \end{cases} \tag{3.7}$$

where h is the altitude in kilometers above mean sea level. The model claims to be valid only above $1.23km$ such that the first line of Equation 3.7 should not be used. The database consisting of night time measurements of the turbulence, this model should be used in the same conditions.

Both static models presented in this section are shown in Figure 3.2. It is clear that, even though the two models are of the same order of magnitude, their shape is quite different, i.e. the layered structure of the C_n^2 is not the same for both models. This is most likely due to the fact that the two models have been developed according to different databases of measurements made at different locations. The tropopause is an atmospheric layer at which an abrupt change in the temperature lapse rate occurs, resulting in an increase in turbulence strength. The altitude of the tropopause is not uniform across the planet and Figure 3.2 suggests that it is around $10km$ for $HV_{5/7}$ and $15km$ for CLEAR 1. Furthermore, the C_n^2 also varies with the seasons such that the profiles might be quite different, in the case the two databases were not constructed at the same time of the year, it could be another explanation of the observed differences.

These static models can be useful because of their simplicity of use but one should keep in mind that they will most likely be valid only if used in circumstances similar to the ones upon which they have been developed. Some models aim at describing turbulence

above high altitude astronomical sites, others above the sea, during night, etc... all might produce quite different C_n^2 vertical profiles.

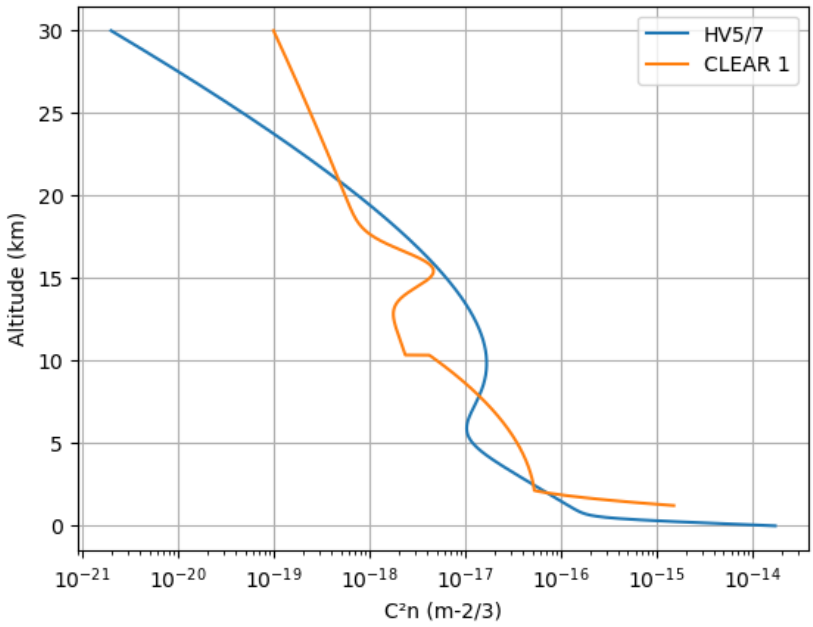

Figure 3.2: $C_n^2(h)$ profile according to $HV_{5/7}$ and CLEAR 1.

3.3.2 Statistical models

Statistical models are based on meteorological parameters such as the temperature, pressure, wind speed, etc... these data are then processed in order to obtain a vertical profile of the refractive index structure constant. They tend to represent the fine structure of the turbulence, i.e. the small fluctuations that are not present in the output of static models. These models rely on the statistical framework of the turbulence developed by Kolmogorov and most of them aim to estimate the outer scale L_0 and then obtain the C_n^2 through Tatarskii's relation Equation 4.4, which has been derived from the study of the microstructure of the concentration of conservative and passive additives in a turbulent flow [23], and in that case, the models distinguish themselves in the way they estimate L_0, as for the three first models of this section. However it is not always the case, some models do not use neither Tatarskii's relation nor the outer scale but rather exploit existing correlations between atmospheric parameters and the turbulence, it will be the case for the last model of this section.

These are less attached to a specific site or climate because the meteorological phenomena responsible for the optical turbulence are loaded at every utilization of the models. They are therefore more reliable and the results are more significant of the region under test as long as one has access to representative atmospheric data. These data often come from routine radiosounding but can also be provided by simulations from Numerical Weather Prediction (NWP) systems such as WRF. While a static model such as $HV_{5/7}$ will always

produce the same profile whatever the location, a statistic model will produce a different output as soon as its inputs change.

Vernin-Tatarskii

The authors in [24] observed thanks to radiosounding data that the median outer scale could be accurately modeled through a decreasing power law within the boundary layer (BL). The parameters of the power law were fitted by minimizing a least squares problem. The complete model for the median outer scale L_0 for the whole atmosphere is given in [23] by :

$$L_0(h) = \begin{cases} 3.21h^{-0.11} & \text{if } h < 1km \\ \frac{4}{1+\left(\frac{h-8500}{2500}\right)^2} & \text{if } 2 < h < 17km \\ 0.307 - 0.0324a + 0.00167a^2 + 0.000476a^3 & \text{if } h > 17km \end{cases} \tag{3.8}$$

where $a = (h/1000 - 17)$ and h is the altitude in meters. This model thus provides a median profile for the outer scale of the turbulence. The computed L_0 can then be plugged in Tatarskii's formula with the rest of the meteorological profiles needed (temperature, pressure and wind speed as functions of the altitude) to produce the vertical structure of the C_n^2. The first line in Equation 3.8 was obtained on the basis of night time measurements (the BL is very sensitive to diurnal variations) [24], therefore one needs to keep that in mind when applying this model to a set of data.

Tjernström

Most information in this section comes from [21]. Here, the outer scale is estimated not simply as a function of the altitude but rather as a function of the Richardson number R_i (defined in Equation 2.12) which is an indicator of a stratified fluid's stability (such as the atmosphere), the C_n^2 is then again retrieved thanks to Tatarskii's relation. The resulting outer scale model is the following :

$$L_0(h) = l\left(1 + 15R_i\sqrt{1+5R_i}\right)^{-1/2} \tag{3.9}$$

where R_i is implicitly a function of the altitude h and l is an asymptotic mixing length in neutral conditions and is set to $23m$ in [21]. Such a model relying on a physical indicator of stability (R_i) seems to have more legitimacy than a fit however the authors did not have access to measured C_n^2 profiles and could not quantify its performances. Furthermore, since the Richardson number is negative around a turbulent layer, Equation 3.9 might present numerical problems when evaluating the square root of a negative number, i.e. when encountering strongly turbulent layers.

WSTG

The WSTG is an improved version of the HMNSP99 model (which depends on the wind shear S and the temperature gradient $\frac{dT}{dh}$ and will be discussed in chapter 4), one of the most widely used statistical models [19]. The authors in [19] have studied the performances

of the model (HMNSP99) according to multiple metrics and observed that they were correlated to the wind shear and the temperature gradient, highlighting poor results in some circumstances. Learning from these statistical observations, they developed a new model (WSTG) which defines the outer scale L_0 in multiple regions of the atmosphere. The key difference resides in the separation of these regions which is not done anymore regarding the tropopause altitude (as is often the case in the literature) but rather depending on the joint values of the wind shear and the temperature gradient.

The model therefore estimates the outer scale L_0 and from there, produces a vertical profile of the C_n^2 according to Tatarskii's formula. The governing equations are the following [19] :

$$L_0^{4/3}(h) = \begin{cases} 0.1^{4/3} \times 10^{0.835 - 37.164S - 306.034\frac{dT}{dh}} & \text{if } S < 0.016 \cap \frac{dT}{dh} < 0 \\ 0.1^{4/3} \times 10^{0.825 + 66.9S - 52.783\frac{dT}{dh}} & \text{if } S < 0.016 \cap \frac{dT}{dh} > 0 \\ 0.1^{4/3} \times 10^{0.715 + 52.907S - 102.515\frac{dT}{dh}} & \text{if } S > 0.016 \cap \frac{dT}{dh} < 0 \\ 0.1^{4/3} \times 10^{2.215 - 9.882S - 101.666\frac{dT}{dh}} & \text{if } S > 0.016 \cap \frac{dT}{dh} > 0 \end{cases} \tag{3.10}$$

The comparison between the two models and the measurements is shown in Figure 3.3 and it appears clearly that the WSTG model performs better in reconstructing the C_n^2 vertical profile. The literature shows multiple examples of models estimating the outer scale with an exponential law such as the one in Equation 3.10 featuring constant coefficients for a given atmospheric layer (usually one expression for the troposphere and one for the stratosphere) and an interesting observation resulting from the performances of the WSTG model is that the dependence of the fitting coefficients on S and $\frac{dT}{dh}$ should be more carefully investigated.

AXP

Most information in this section comes from [23]. This model is based on the knowledge that optical turbulence occurs most of the time in thin twin layers or laminae due to strong potential temperature gradients. From there, and thanks to a large database of night flights of balloons equipped with thermosondes in the Canary Islands and Chile, the authors estimate the temperature structure constant as follows :

$$C_T^2(h) = \langle C_T^2(h) \rangle \left(A(h) \frac{\partial \bar{\theta}}{\partial h} \right)^{p(h)} \tag{3.11}$$

where $\langle C_T^2(h) \rangle$ is the median profile of the temperature structure constant, $\bar{\theta}$ is the mean potential temperature and $p(h)$ and $A(h)$ are the two altitude dependent coefficients of the AXP model. The temperature structure constant is supposed to follow a median profile modulated by the mean potential temperature gradient. The intensity of the peaks are defined by the power $p(h)$ while $A(h)$ defines their altitudes.

The two coefficients were obtained by minimizing the euclidean distance :

$$d_\epsilon(h_i) = \sum \left(\epsilon_r(h_i) - \epsilon_{AXP}(h_i) \right)^2 \tag{3.12}$$

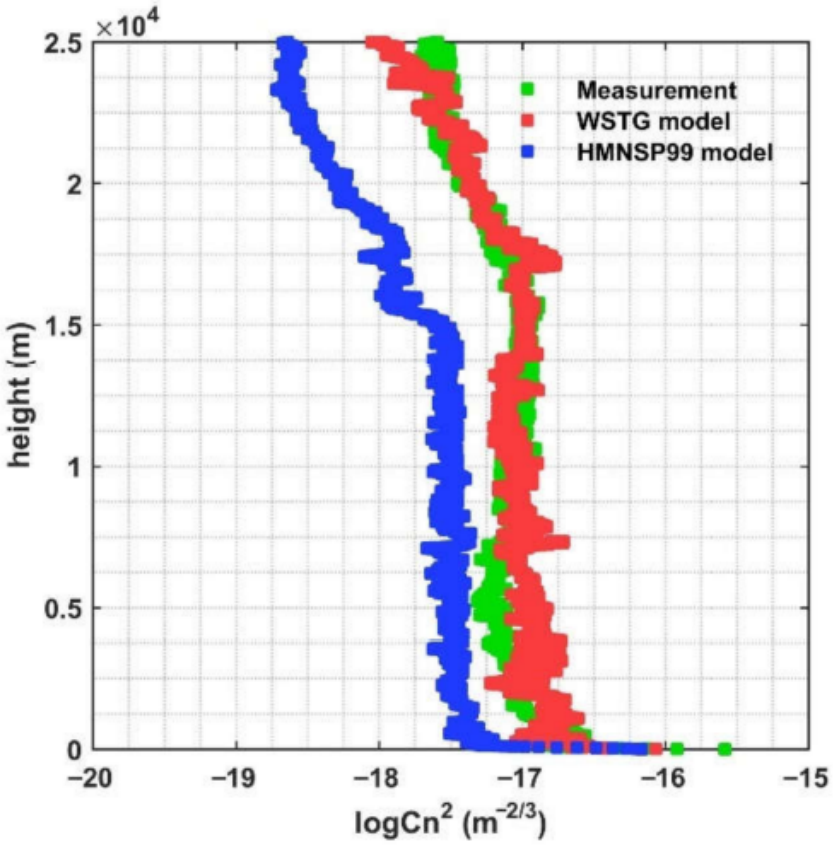

Figure 3.3: Comparison between HMNSP99, WSTG and measurements [19].

where the sum is carried over all the flights from the database and $\epsilon_r(h_i)$ and $\epsilon_{AXP}(h_i)$ are the recorded and estimated local seeing respectively. The local seeing is defined as :

$$\epsilon(h_i) = 5.25\lambda^{-1/5} \left(\int_{h_i-500}^{h_i+500} C_n^2(z)dz \right)^{3/5} \tag{3.13}$$

Once the temperature structure constant has been estimated, the C_n^2 is obtained thanks to Gladstone's formula Equation 2.10. This model does not involve neither Tatarskii's relation nor the outer scale of the turbulence. It is valid throughout the whole atmosphere and is based upon night time data and should therefore be used in such conditions.

3.3.3 Numerical models

Numerical models estimate the optical turbulence parameters by solving complex sets of differential equations on a grid. They are usually more accurate than static and statistic models but they are also much more complex both in their definition (the equations to solve), initialisation (the input data needed to launch the simulation) and execution (the time needed to produce a result). However, despite this complexity, they are of great interest for site testing as well as flexible scheduling [11, 25].

Meso-NH

Most information in this section comes from [25]. The Mesoscale Non-Hydrostatic is a numerical model developed by Masciadri et al. in [25] in an attempt to overcome the restrictions inherent to in-situ measurement campaigns, i.e. expensive, need a lot of man-power, at only one site and one line-of-sight and have no predictive capability.

The model needs to be initialized with a numerical terrain model with a high spatial resolution as well as the fields of atmospheric pressure, temperature, humidity and wind at a given initial time t_0. The atmospheric fields can originate from either radiosoundings from meteorological stations or, most likely, from reanalysis data (e.g. ERA5 from ECMWF see chapter 6 for more details about the reanalysis data). From there, the model will produce a 3D map of the refractive index structure constant C_n^2 as well as other integrated parameters. The model relies mainly on the turbulence kinetic energy equation to link microscopic quantities such as the vertical potential temperature fluctuations to the the macroscopic variables. The final objective of the model is to compute the potential temperature structure constant and then retrieve the C_n^2 with Gladstone's formula Equation 2.10.

The model has been compared to SCIDAR measurements and the two profiles are shown in Figure 3.4 and are in close agreement. The execution time to reach those results was of about 4 hours. It appeared that this numerical model is able to produce high quality estimations of the C_n^2 in a 3D grid, which is not possible today with the current measurement techniques, it aims at replacing the expensive and tedious measurement campaigns in case of site testing. Moreover, the authors expect it to bring a contribution in the frame of flexible scheduling. However, the execution time is non-negligible and vastly superior to the ones of the static and statistical models.

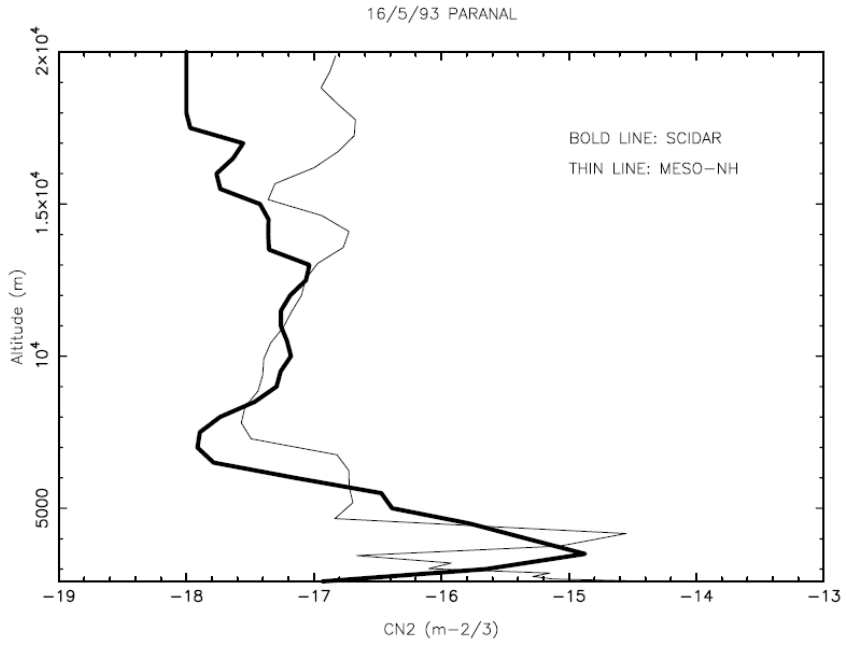

Figure 3.4: Meso-NH and SCIDAR measured C_n^2 profiles at Paranal mountain [25].

This chapter has first presented the main optical turbulence-related parameters others than the C_n^2. They were characterized by their mathematical expressions and an interpretation of each of them was also given to motivate their importance mainly in adaptive optic systems.

Then, the principal instruments measuring these parameters were introduced along with their working principles/equations. Each of them having its own advantages and drawbacks and measuring its own set of parameters : some measure the seeing, others the C_n^2 itself, with a good/poor temporal and/or spatial resolution, etc... The main common drawback about these instruments is that they are expensive, need human work force (sometimes substantial), only measure part of the optical turbulence-related parameters and can only provide them along a unique line of sight. This motivates the use of estimation models.

The estimation is a cheaper and easier manner to get the vertical profile of the C_n^2 and many models have been developed throughout the years. Static models are very easy and need most of the time only the altitude as input, they produce smooth and generalized trendlines depending highly on the atmospheric conditions relative to the measurement campaign upon which they are based. Numerical models are much more complicated regarding the equations, the inputs and has a long execution time (several hours) but produce accurate 3D profiles. Finally the statistical models are a good trade-off between complexity and performance, they rely mainly on Tatarskii's formula or exploit the existing correlation between the temperature (or potential temperature) structure constant and classical atmospheric parameters. Because they represent such an interesting trade-off, three additional statistical models will be presented and discussed in depth in the following chapters.

Chapter 4

Studied models

As was already explained, the statistical models usually provide a good trade-off between complexity and performance which is why three of them were selected for an in-depth study. Two of the models rely on Tatarskii's formula Equation 4.4 while the third one exploits the correlation between the potential temperature structure constant and the buoyancy and windshear. This chapter will provide a description as complete as possible of the different models and their origins.

4.1 Trinquet & Vernin

The model proposed by Trinquet and Vernin in [26] exploits the existing correlation between the fluctuations of the temperature structure constant C_T^2 (or potential temperature structure constant, the two being often used interchangeably in the literature) and the ones of the gradient of mean potential temperature $\frac{\partial\theta}{\partial h}$ (or buoyancy χ) as well as the shear of the horizontal wind speed S with u and v being the two horizontal wind speed components (Equation 4.1). The refractive index structure constant C_n^2 is then retrieved thanks to Gladstone's formula Equation 2.10 (where it is accepted that $C_\theta^2 = C_T^2$). This model was developed according to a statistical study performed over 145 flights of meteorological balloons equipped with micro-thermal sensors (i.e. thermosondes), from the ground up to mid-stratosphere. It is important to note that all the flights were launched during the night since day time and night time C_n^2 profiles are not identical.

$$S = \sqrt{\left(\frac{\partial u}{\partial h}\right)^2 + \left(\frac{\partial v}{\partial h}\right)^2} \tag{4.1}$$

The model relies on the following mathematical expression :

$$C_T^2 = \phi(h)\chi(h)^p S(h)^q [26] \tag{4.2}$$

where $\phi(h)$ is a function regrouping the values of the median profiles of C_T^2, S and χ from the 145 flights constituting the database and can be found in [11] but for simplicity, it is reproduced in Figure 4.1. A bivariate least-squares fit is performed over the logarithmic fluctuations of the estimated and observed C_T^2 from the database in order to determine p and q. Finally the model can be expressed as :

$$C_T^2 = \phi(h)\chi(h)S(h)^{1/2} \tag{4.3}$$

Since both C_T^2 and S are positive quantities, only portions of the atmosphere where $\chi > 0$ are considered. Convective regimes were excluded and rarely occurred among nighttime profiles [26]. The authors noticed that the model is sensitive to the vertical resolution, which is a phenomenon that has been also observed in this work and will be discussed later. Finally it is interesting to note that, unlike models using Tatarskii's relation, this one does not imply the outer scale of the turbulence L_0.

Couche limite		Atmosphère libre	
Altitude (m)	ϕ	Altitude (m)	ϕ
5	2.8349920	1500	0.2202239
55	0.7825773	2500	0.1232994
105	0.2851246	3500	0.1220847
155	0.2247893	4500	0.1116992
205	0.2339369	5500	$7.9565063 \cdot 10^{-2}$
255	0.2368697	6500	$7.6611020 \cdot 10^{-2}$
305	0.1393718	7500	$9.4689481 \cdot 10^{-2}$
355	0.1697904	8500	$8.2437001 \cdot 10^{-2}$
405	0.1350916	9500	$8.5563779 \cdot 10^{-2}$
455	0.1151705	10500	$7.9648279 \cdot 10^{-2}$
505	0.1201656	11500	$5.9562359 \cdot 10^{-2}$
555	0.1242000	12500	$4.4496831 \cdot 10^{-2}$
605	0.1528365	13500	$4.5322943 \cdot 10^{-2}$
655	0.1258108	14500	$3.8577948 \cdot 10^{-2}$
705	0.1038473	15500	$4.9237989 \cdot 10^{-2}$
755	$9.6003376 \cdot 10^{-2}$	16500	$4.5535788 \cdot 10^{-2}$
805	$8.3205506 \cdot 10^{-2}$	17500	$4.5892496 \cdot 10^{-2}$
855	0.1061958	18500	$3.9653547 \cdot 10^{-2}$
905	$9.4715632 \cdot 10^{-2}$	19500	$4.1269500 \cdot 10^{-2}$
955	0.1022552		

Figure 4.1: Vertical profile of ϕ deduced from the statistical analysis of balloons sounding [11].

4.2 Dewan (or AFGL)

This model proposed by Dewan et al. in [27], valid above the boundary layer (but often used for the whole atmosphere), will give the turbulence strength as a function of standard radiosonde data. It relies on Tatarskii's relation :

$$C_n^2 = aM^2 L_0^{4/3} \tag{4.4}$$

where a is a constant most often set to 2.8 [28, 9], $M = -\frac{79*10^{-6}P}{T}\frac{\partial \ln\theta}{\partial h}$ [9] is the vertical gradient of the potential refractive index gradient ([27] uses a slightly different expression with T and the dry adiabatic lapse rate instead of θ but the results are identical here) and L_0 is the outer scale of the turbulence, P is the pressure in mb and T is the absolute temperature in K. The true unknown in Equation 4.4 is L_0 and it is precisely what the

model aims at providing.

It is generally known that, in the free atmosphere (i.e. above the boundary layer) optical turbulence appears in thin laminae that are kilometers wide and a few tens of meters thick. Those laminae are usually due to *gravity waves*, caused by meso-scale atmospheric phenomena (e.g. the jet stream) or large orographic disturbances (e.g. mountains) [27, 4]. Dewan and Good established an unstability criterion as :

$$S_c^2 > N^2(0.5)^{-1} \tag{4.5}$$

where $N^2 = \frac{g}{T}\frac{\partial\theta}{\partial h}$ is the Brunt-Vaissala frequency [4], such that all shear regions exceeding $S_c = 0.015s^{-1}$ in the troposphere and $S_c = 0.03s^{-1}$ in the stratosphere are supposed turbulent. The authors in [27] suggest that the outer scale L_0 is of the order of 1/10 the thickness of the turbulent layer ($\mathcal{L}$), this assumption will be taken into account when writing the final expression of the model Equation 4.8.

Radiosonde data at the time the model was published (1993) had a resolution of minimum $300m$ which is about one order of magnitude higher than the thickness of a turbulent layer and the instability criterion Equation 4.5 is very rarely met. Furthermore, it is expected that the shears responsible for the instability would be of the same scale as the turbulent layers. Van Zandt et al. [29] pointed out the importance of describing the small-scale fluctuations of the required meteorological quantities in terms of the measurable large-scale available data. A statistical association is needed between the large-scale available radiosonde data, S_{RAW}, and the average L_0 contained within the $300m$ height range, based on the small-scale but unmeasurable (at the time !) shears. This statistical association has been obtained by the authors in [27] thanks to very high resolution ($\approx 10m$) velocity profiles from stratospheric rocket laid smoke trails.

The procedure to assign the value of the S_{RAW} to the average $\mathcal{L}$, and then L_0, is illustrated in Figure 4.2. Thanks to the high resolution profiles, it has been possible to obtain the altitude profile of the wind shear S and all regions exceeding S_c are considered turbulent such that it is possible to to assess their thicknesses. The average thickness is given by the following expression :

$$\langle \mathcal{L}_i^{4/3} \rangle = \sum \mathcal{L}_i^{4/3} \left(\frac{\mathcal{L}_i}{290} \right) \tag{4.6}$$

S_{RAW} is then obtained by smoothing the velocities and differentiating over $300m$ and finally, plotting the thickness as a function of S_{RAW} gives the two graphs in Figure 4.3 from which the authors obtained the following linear regressions for $Y = \log(\langle \mathcal{L}_i^{4/3} \rangle)$ (the maximum shear used in the regression was $0.045s^{-1}$) :

$$\begin{aligned} Y &= 1.64 + 42S_{RAW} \quad Troposphere \\ Y &= 0.506 + 50S_{RAW} \quad Stratosphere \end{aligned} \tag{4.7}$$

The model is now finally complete and can be written as :

$$C_n^2 = aM^2(0.1)^{4/3}10^Y \tag{4.8}$$

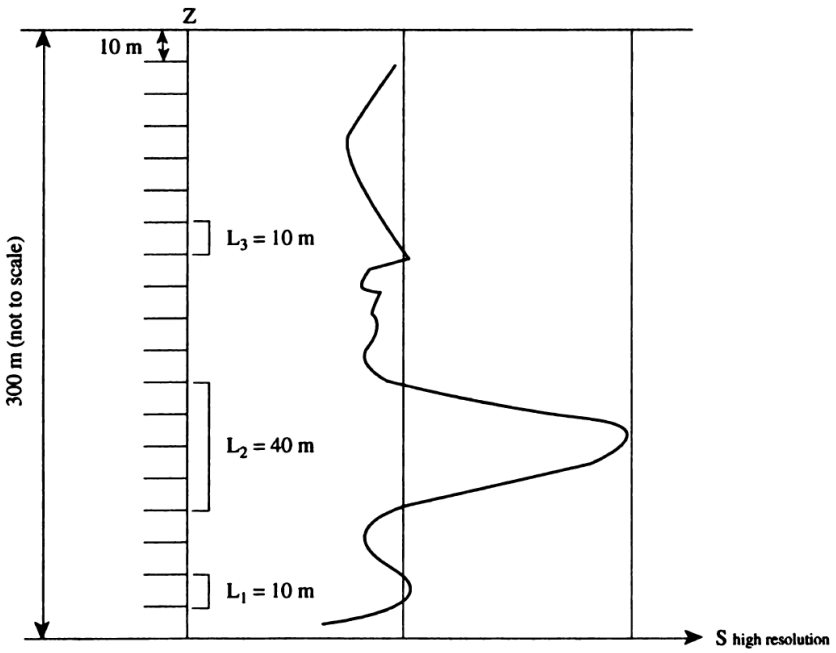

Figure 4.2: Method for assigning S_{RAW} to $\langle \mathcal{L} \rangle$ [27].

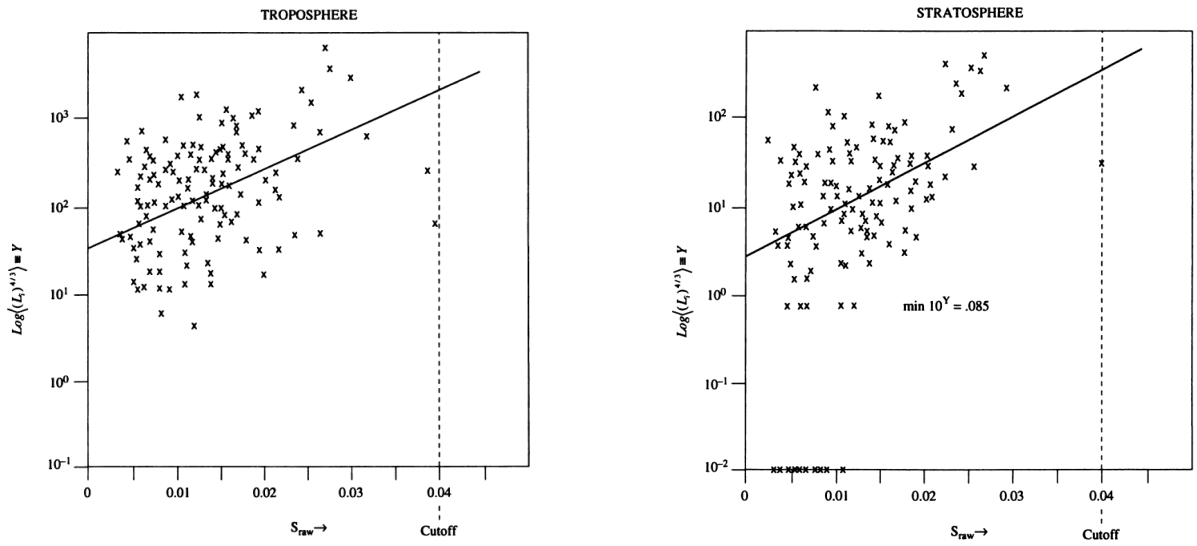

(a) Tropospheric regression ($S_c = 0.015s^{-1}$). (b) Stratospheric regression ($S_c = 0.03s^{-1}$).

Figure 4.3: 10^Y vs S_{RAW} regression [27].

4.3 HMNSP99

Ruggiero & DeBenedictis developed an outer scale model at the Air Force Research Laboratory from the Holloman Spring 1998 and Holloman Spring 1999 thermosonde campaigns (HMNSP99), which gave the relationship relating the outer scale L_0 to the wind shear and the temperature gradient [19]. Unfortunately, the document relative to this research was not available and a deep description of the model's origins could not have been obtained, unlike TV and Dewan models. No information could be found on the interval of validity

of this model but [9, 19] use it from the ground up to $30km$. However, poor results in terms of RMSE in the first few hundreds of meters (see Figure 5.10b) suggest that this model is not best suited to describe optical turbulence within the boundary layer.

This model also relies on Tatarskii's relation Equation 4.4 and aims at providing an accurate estimation of the outer scale L_0 in a similar way as Dewan et al. [27] but including the temperature gradient as well. The resulting expression is [9, 19]:

$$\begin{aligned} L_0^{4/3} &= 0.1^{4/3} \times 10^{0.362+16.728S-192.347\frac{\partial T}{\partial h}} \quad Troposphere \\ L_0^{4/3} &= 0.1^{4/3} \times 10^{0.757+13.819S-57.784\frac{\partial T}{\partial h}} \quad Stratosphere \end{aligned} \tag{4.9}$$

Again, the expression of L_0 depends on whether the considered altitude is above or below the tropopause. This expression rose from the statistics linking the outer scale to the wind shear and temperature gradient [19]. Equation 4.9 being very similar to the expression of the outer scale developed by the authors in [27] (0.1 factor, exponential of wind shear) it seems fair to say that it must rely on an analogous reasoning (this model has been developed less than 10 years after Dewan's).

The three different statistical models were investigated and one can already sense that some parameters such as the spatial resolution of the input data will have an impact on the resulting refractive index structure constant vertical profile. These models depend on standard meteorological parameters widely available and have been developed according to very large databases. The next chapter will discuss individually the performances of each of the three models and investigate the origins of some characteristic behaviours in the output profile.

Chapter 5

Results and discussion

This master thesis benefited from the T-REX measurements campaign which measured multiple vertical profiles of the C_n^2 as well as standard meteorological parameters thanks to thermosonde-equipped balloons. This allowed to assess the performances of the three models in their reconstruction of the vertical profile of the refractive index structure constant according to a certain metric. Furthermore, it is possible to check the impact of the data filtering on the performances of each model. Finally, a suggestion for detecting and reducing the number of outliers in the outer scale estimation is presented.

5.1 T-REX measurement campaign

The T-REX measurement campaign objectives, inter alia, were to study higher altitude mountain waves (i.e. gravity waves) and the associated turbulence. Both radiosonde (classical atmospheric parameters) and thermosonde (mainly the temperature structure constant) data were recorded during the campaign. The thermosonde allows to directly measure the temperature structure constant C_T^2 (assuming that the turbulence follows the Kolmogorov's behaviour) and from there, obtain the refractive index structure constant C_n^2 through Gladstone's formula Equation 2.10. The instruments were launched from the windward side of the Sierra Nevada, near Three Rivers California, between March 22, 2006 and April 6 of the same year [30]. Those thermosonde data regroup the following quantities from roughly $h = 500m$ up to $h = 28km$ on average :

- Temperature T
- Pressure P
- Wind speed w
- Wind direction α
- Relative humidity RH (never used by the three models)
- Refractive index structure constant C_n^2

15 satisfactory flights were recorded during this period of time, giving as many data sets of the previous quantities. These atmospheric parameters can then be used as inputs to

the different models and their outputs will then be compared to the measured C_n^2 in order to assess their performances according to some metric yet to be introduced. Furthermore, these data will allow an in-depth understanding of the behaviour of the models i.e. outlier sources, relative importance of the inputs, measurement noise impact, etc... in order to be able to do a critical analysis of the results produced by the models when no measured C_n^2 profiles are available.

All of the non-static models that will be discussed rely on atmospheric parameters such as the profiles shown in Figure 5.1 and their gradients (except for the pressure). The two horizontal wind speed components from Figure 5.1c (u and v) are given by :

$$u = w \cos \alpha \tag{5.1}$$

$$v = w \sin \alpha \tag{5.2}$$

One last comment, [30] shows a similar tropopause altitude $h_{trop} \approx 12km$ as the one computed here. This altitude is of critical importance for Dewan and HMNSP99 models which use different outer scale expressions according to the altitude, whether it is above or under h_{trop}. The tropopause is the boundary that demarcates the troposphere from the stratosphere. It is characterized by an abrupt change in the temperature gradient and is defined as the first altitude where $\frac{\partial T}{\partial h} > 0.002K/m$ if the gradient remains positive within a $2km$ thick layer above the given altitude [31].

5.2 Metric of performance

The metric of performance considered here is the Root Mean Square Error (RMSE), defined as :

$$RMSE = \sqrt{\frac{1}{N} \sum_{i}^{N} (X_i - Y_i)^2} \tag{5.3}$$

where X_i is the actual value of a parameter and Y_i is the estimated value of the same parameter, N is the number of profiles used to compute the sum (i.e. the number of T-REX data sets). Because the C_n^2 varies of multiple orders of magnitude from day to day and from one altitude to another, $X_i = \log_{10}(C_n^2(h))$. This metric will also be applied to the integrated parameters in chapter 6.

5.3 Trinquet & Vernin

Both the measured and predicted C_n^2 profiles are shown in Figure 5.2. The mean profiles from Figure 5.2 have been averaged over all the individual profiles coming from the 15 different data files from the T-REX measurement campaign.

The model has been applied to radiosonde data which have the finest vertical resolution among all measurement techniques ($\approx 10m$), but present a main drawback, i.e. the increased noise level. This noise will be further amplified by the derivatives [32] present in the mathematical expression of the model Equation 4.3, through the temperature gradient

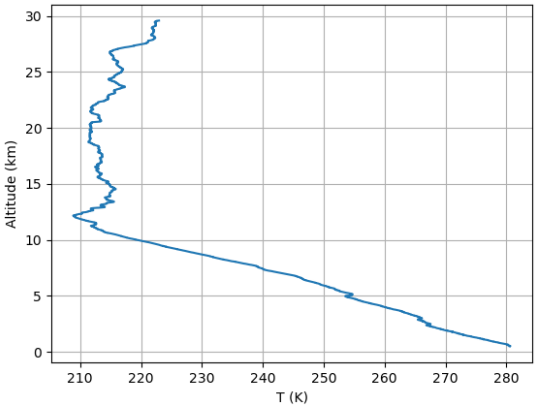

(a) Temperature.

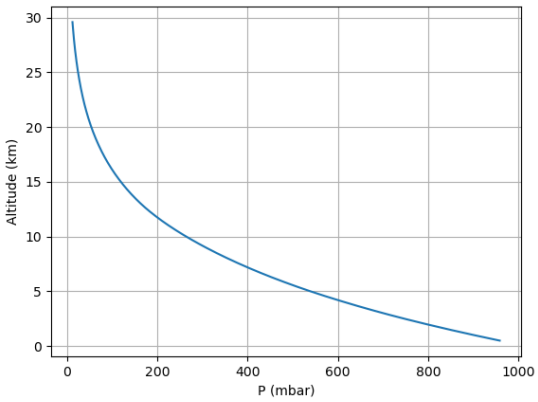

(b) Pressure.

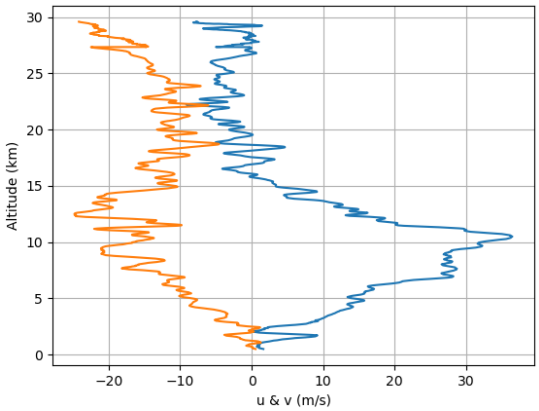

(c) Horizontal wind speed components.

Figure 5.1: Vertical profiles of some atmospheric quantities from the T-REX measurement campaign.

implicitly present in χ, and the wind shear.

One solution to reduce the impact of noise on the results is to filter the input data before anything else. This can be done in various ways and here the data points have been gathered in bins of a given size B (i.e. B is the number of samples in one bin) and only their average is kept. The remaining points are interpolated in order to keep the size of the data vectors constant throughout processing. The higher B, the more averaging and hence the less noise. Figure 5.3 shows the impact of filtering the input data on both the data itself (T here) and its derivative. The relative difference between a quantity N and its filtered version N_f is defined as :

$$|\frac{N - N_f}{N}|$$

and by setting $N = T$ and $N = \frac{\partial T}{\partial h}$ (careful that only T is filtered and never its gradient but it is then computed with the filtered T, the difference is subtle but important) successively one can observe one to two orders of magnitude difference between them, hence filtering is critical when evaluating derivatives.

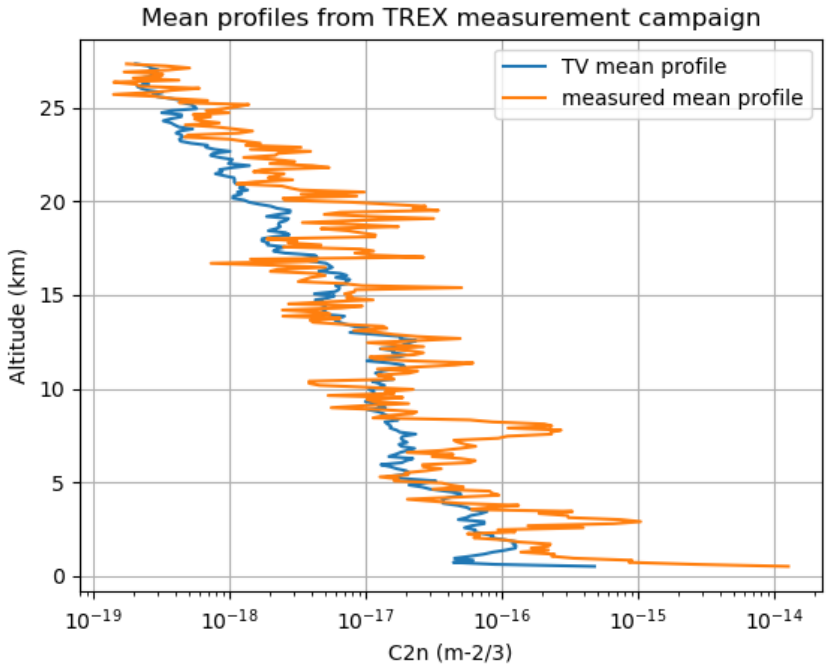

Figure 5.2: C_n^2 vertical profile from measurements and predicted by the TV model with a bin size of 5.

To quantify the impact of the filtering on the quality of the results, a new scalar metric of performance is introduced, i.e. the *mean Root Mean Square Error* defined as :

$$\mu_{RMSE} = \frac{1}{N} \sum_{i=1}^{N} RMSE(h_i) \tag{5.4}$$

which is a mean RMSE averaged over the heights going from $h_1 \approx 500m$ up to $h_N \approx 27.5km$. This window corresponds to the altitudes where data are available for all the data files from the TREX measurement campaign. This new scalar metric of performance aims at giving an easier way to compare quantitatively multiple C_n^2 profiles. It is now possible to plot the μ_{RMSE} as a function of the bin size parameter B, as in Figure 5.4a. To further ease the reading of the plot, it has been normalized by the value of μ_{RMSE} when the input data have not been filtered ($B = 1$). The bin size in meters can be approximately obtained by $10B$, giving an idea of the resulting spatial resolution.

Figure 5.4a clearly shows that there is an optimal bin size $B_{opt} = 128$ for which the μ_{RMSE} is minimum ; the noise is still strongly present for lower bin sizes while information is lost when B becomes too large. However it is also important to notice that the gain in μ_{RMSE} from $B = 2$ to $B_{opt} = 128$ is only roughly 2% and that the maximum gain due to filtering barely exceeds 7%. Having access to only 15 daily profiles from the TREX campaign it is not safe to consider Figure 5.4a as reference for the optimal vertical resolution but rather a confirmation that filtering does impact the performances of the model. In order to define the parameters p and q from Equation 4.2, the authors in [26] use a $100m$ linear regression to compute the gradients which is relatively similar to a second order centered differences method with a resolution of 50m, corresponding to $B = 5$, used here, but they tested

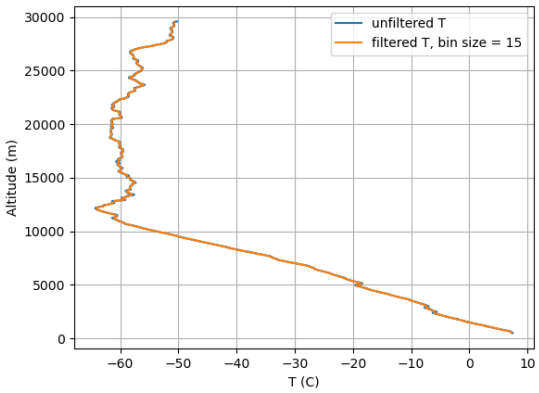

(a) $T(h)$.

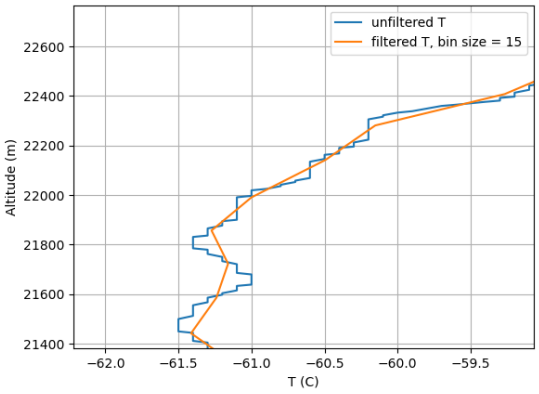

(b) $T(h)$ zoom.

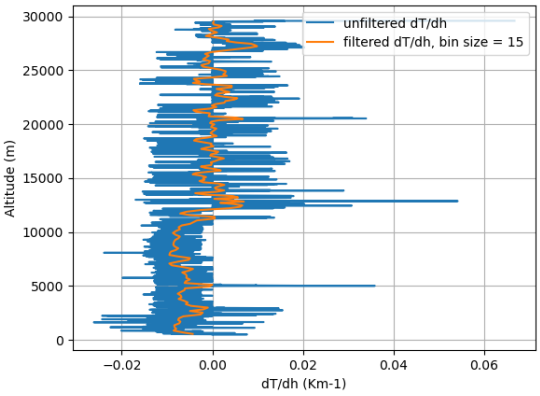

(c) $\frac{\partial T}{\partial h}$.

Figure 5.3: Impact of binning on the vertical profiles of temperature T and temperature gradient $\frac{\partial T}{\partial h}$.

it with gradients computed over $300m$, corresponding roughly to $B = 15$, therefore the results seem coherent. It appears that TV is sensitive to the vertical resolution, as said in [26], but the noise present in the measurements has a limited impact on the performances of the model. Filtering mainly reduces the number of extreme values (mostly outliers) and reduces the oscillations (thinner curve), as can be seen in Figure 5.4b (here B is taken high enough such that the effects of filtering can easily be seen). Finally the RMSE for a bin size $B = 5$ is plotted in Figure 5.4c and shows that the worst performances of the model appear in the first few hundreds of meters, within the boundary layer. Some possible explanations would be the following. The turbulence in this layer is particularly difficult to describe and is mainly governed by the heat flux between the ground and the atmosphere, the orography, etc... and most of the models treat it as a different case, unlike TV. Furthermore TV has been developed according to a database of nighttime flights while half of the data files from the TREX campaign correspond to flights launched around 2:00 UTC (which is 6pm at Three Rivers, California), which might not be considered as nighttime. Indeed the behaviour of the C_n^2 in the boundary layer is very different from day to night conditions.

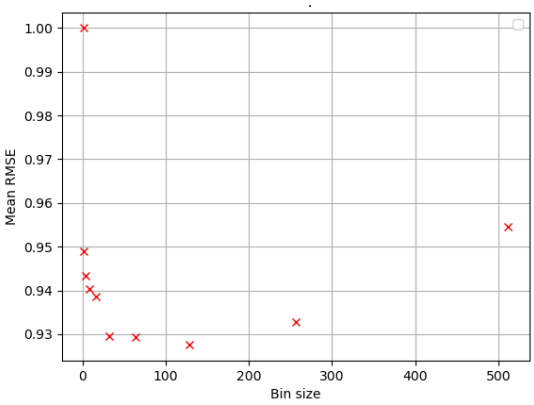

(a) Normalized μ_{RMSE} as a function of the bin size parameter B.

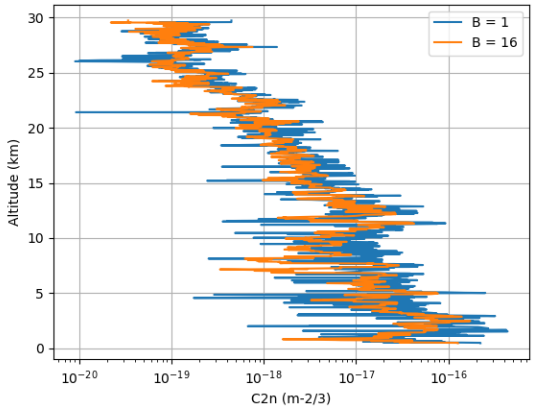

(b) Comparison on one daily profile estimated with ($B = 16$) and without ($B = 1$) filtering.

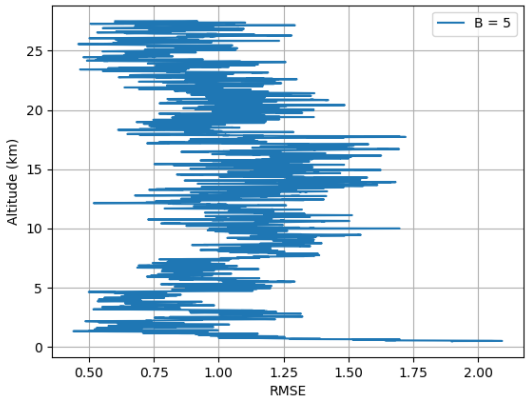

(c) RMSE of TV with $B = 5$.

Figure 5.4: Impact of the bin size parameter B on the performances of TV.

5.4 Dewan (or AFGL)

The plots of the mean profiles (measured and estimated) as well as the RMSE are shown in Figure 5.6. The authors of the model were very clear about the vertical resolution of the data to use and strongly recommend to stick to $300m$, arguing that a model should be intended for a particular data format. Indeed, many considerations in the development of the model came from the fact that the available resolution was not able to directly reflect the small-scale fluctuations and hence the statistical study. Forcing the vertical resolution to $300m$ already acts as a kind of filter since the fluctuations of smaller scales than the resolution cannot be taken into account. Therefore no study about filtering was done in this section and the data were artificially reduced to a resolution of $300m$.

Some comments and warnings can be formulated at this stage. The high resolution vertical profile of S_{RAW} used for the statistical association were only obtained in the stratosphere and the authors themselves agreed that it was a weak assumption to suppose that the stratospheric and tropospheric shear statistics do not differ significantly. This could be reflected in poorer RMSE below the tropopause ($h_{trop} \approx 12km$ according to

the temperature profiles from TREX) in Figure 5.6b. Furthermore the authors did not intend to represent the optical turbulence within the boundary layer so one should be very cautious when discussing the lower part of the atmosphere according to this model, specially when estimating the *coherence length* r_0 which is very sensitive to the first kilometers above ground. To overcome this, the authors in [27] have extended their model with some others when concerned with the boundary layer. Finally, a word regarding the case where the model is applied to raw radiosonde data with a resolution of about $10m$. As said before, higher resolution data record more noise and this noise is amplified by the computation of the wind shear S through the gradient of the wind speed. With such data, S can take values up 40 times higher which translates to outrageous values of the outer scale L_0 as shown in Figure 5.5. The authors fixed a limit on the maximum acceptable shear $S_M = 0.04s^{-1}$ when applying the model to measurements because a single outlier could totally dominate the C_n^2 profile. They also fixed a condition regarding the temperature gradient in the troposphere which should never exceed $10^{-6}Km^{-1}$. This rises the idea of setting thresholds on the acceptable values of the outer scale, which will be developed further in this text.

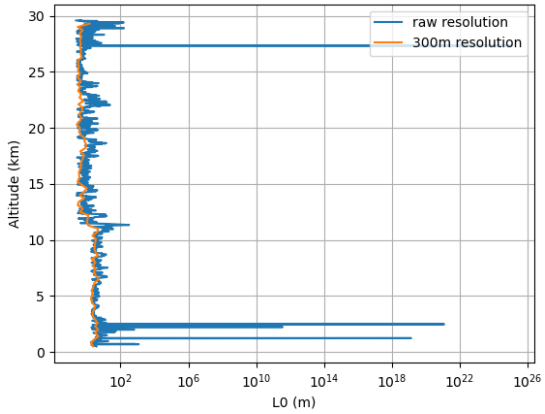

(a) Estimated L_0 with raw data and a $300m$ resolution.

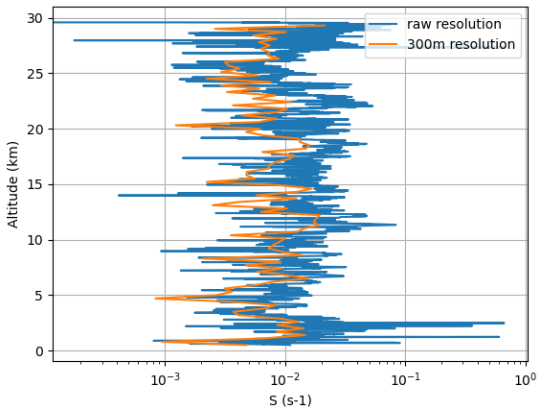

(b) S computed with raw data and a $300m$ resolution.

Figure 5.5: Comparison of data resolution on S and L_0 computed with Dewan's model.

5.5 HMNSP99

The measured and estimated mean profiles are shown in Figure 5.9b.It is interesting to have a look at the impact of data filtering on the computed temperature gradient and wind shear, as shown in Figure 5.7. It appears that temperature is more sensitive to filtering than wind speed, showing often a factor of 2 between the filtered ($B = 5$) and unfiltered cases. Since $\frac{\partial T}{\partial h}$ and S are globally of the same order of magnitude, i.e. 10^{-3}, and because of the corresponding coefficients in the exponential term of Equation 4.9, the outer scale of HMNSP99 model is extremely sensitive to filtering through the temperature gradient. Furthermore, $\frac{\partial T}{\partial h}$ taking both positive and negative values, it can produce very large-valued outliers of L_0 as well as very small-valued ones, unlike S which can only contribute to large-valued outliers since it can only be positive. The respective

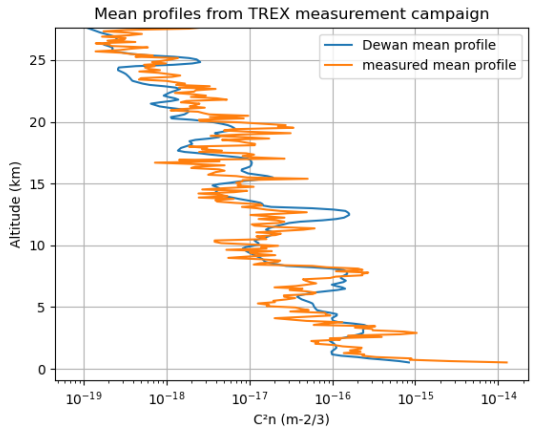

(a) Measured and estimated (with Dewan model) mean C_n^2 profiles.

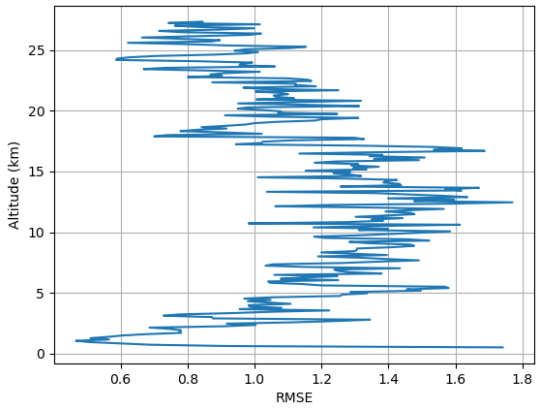

(b) RMSE of Dewan model.

Figure 5.6: Results of Dewan model applied to the data from the TREX measurement campaign.

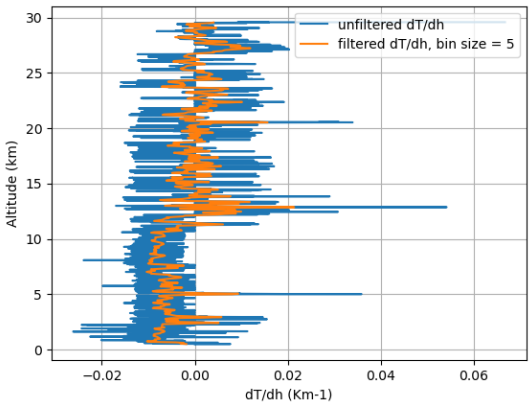

(a) Impact of filtering on $\frac{\partial T}{\partial h}$, $B = 5$

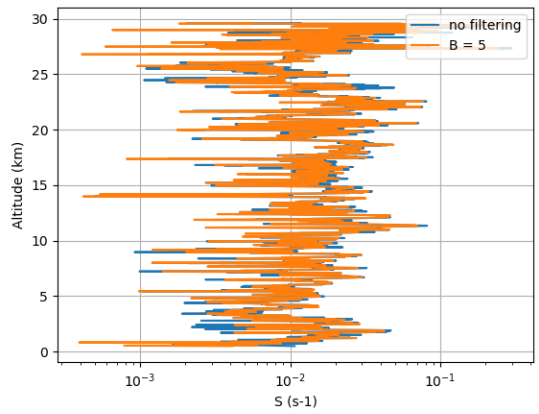

(b) Impact of filtering on S, $B = 5$

Figure 5.7: Impact of filtering temperature and wind speed on $\frac{\partial T}{\partial h}$ and S respectively.

contributions of $\frac{\partial T}{\partial h}$ (i.e. $-192.347\frac{\partial T}{\partial h}$ in the troposphere) and S to the argument of the exponential term in Equation 4.9 are shown in Figure 5.8 (with a B similar but not exactly identical to the one in Figure 5.7). This highlights the fact that the outer scale is more dependent on the temperature gradient in the troposphere while the contributions of $\frac{\partial T}{\partial h}$ and S are quite of the same magnitude in the stratosphere. It is now interesting to have a look a the vertical profile of the outer scale with and without filtering, as shown in Figure 5.9a. Filtering the data produces a thinner curve (less oscillations) with less outliers.

Finally, it is once more interesting to assess quantitatively the impact of filtering according to a scalar metric of performance, i.e. the μ_{RMSE}. The graph in Figure 5.10a shows a similar shape as the one in Figure 5.4a for TV but the gain due to filtering is much more visible (up to 20%) and the optimal bin size is now $B_{opt} = 64$. Again, this should not be regarded as a formal proof that the optimal bin size is indeed 64 but rather that an optimum exists and that it should lie around this value. Furthermore the gain between

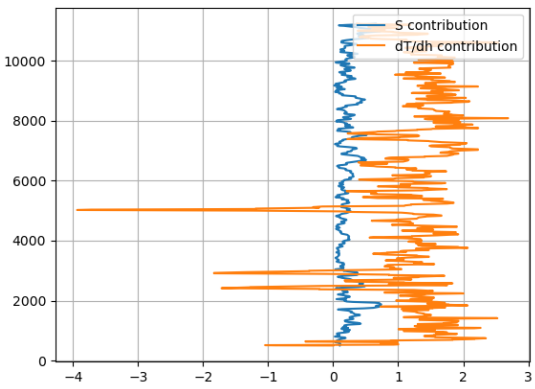

(a) Troposphere

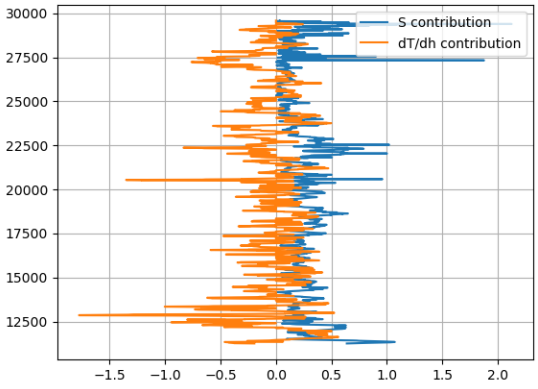

(b) Stratosphere

Figure 5.8: Contributions of $\frac{\partial T}{\partial h}$ and S to L_0 (computed with HMNSP99) in both the troposphere and the stratosphere.

$B = 8$ and $B = 64$ is of about 2% only and the $300m$ resolution specific to Dewan falls within this interval. This seems coherent given the similarity between the outer scale models of both Dewan and HMNSP99.

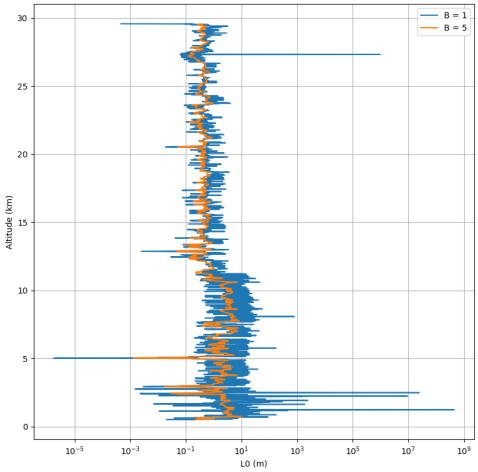

(a) L_0 with ($B = 5$) and without ($B = 1$) filtering. Computed with HMNSP99.

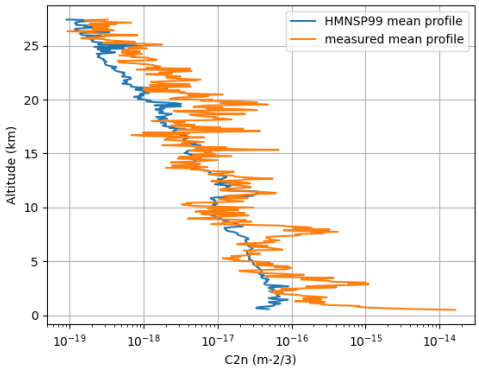

(b) Measured and estimated (with HMNSP99) mean C_n^2 profiles ($B = 64$).

Figure 5.9

5.6 L_0 outlier detection

The outer scale L_0 is of primary importance when discussing turbulence and its numerical evaluation sometimes gives rise to absurd values. Filtering highly impedes the apparition of such outliers but still, it raises the question : *What is an absurd value of* L_0 *?* The answer to that question could provide an additional safety net to the different models,

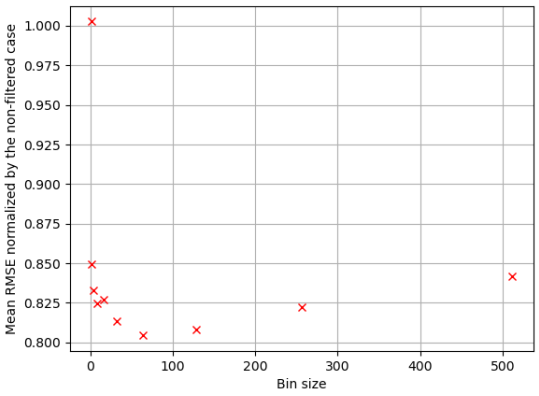

(a) Normalize μ_{RMSE} as a function of the bin size B.

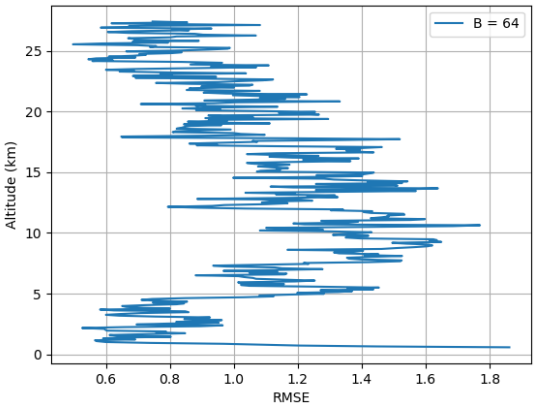

(b) RMSE of HMNSP99 with $B = 64$.

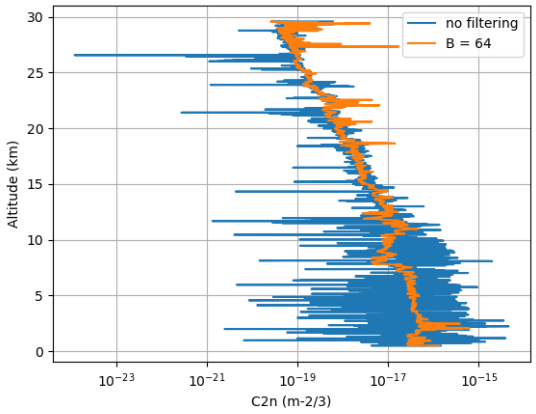

(c) Daily profile with ($B = 64$) and without ($B = 1$) filtering.

Figure 5.10: Impact of the bin size B on the performances of HMNSP99.

allowing them to spot outliers and discard them.

If L_0 follows a certain statistical distribution, a natural way to define the outliers would be the points that do not belong to a given interval of confidence (e.g. the 98% confidence interval). Reversing Tatarskii's relation Equation 4.4 in order to isolate the outer scale as a function of the measured C_n^2 from the T-REX measurement campaign, one obtains the vertical profile of the "measured" outer scale L_0 ("measured" is not really the most appropriate word since one did not actually measure L_0 but it is used here to emphasize on the fact that it comes from a measured C_n^2 profile). This profile (that has been obtained with only one C_n^2 profile) can then be used to define the statistical distribution of L_0, which is shown in Figure 5.11.

The outer scale seems at first sight to follow a bimodal log-normal distribution but no statistical test were performed to ensure it. The red curve in Figure 5.11 suggest that the distribution is gaussian and the second smaller peak centered around 0 implies that the distribution has more than only one mode. This is coherent with the plots of L_0 clearly showing a mean value between 1 and 10 in the troposphere and another mean

value between 0.1 and 1 in the stratosphere. These mean values are the two modes of the distribution.

This bimodal distribution suggests that two classical log-normal distributions, depending on whether the altitude of interest is above or under the tropopause, could be used to detect outliers. An interesting lead for future work would therefore be to investigate the statistical distribution of the outer scale in more localized atmospheric layers (and not the whole $[0km : 30km]$ layer at once) like the troposphere and the stratosphere separately and using more than only one C_n^2 profile.

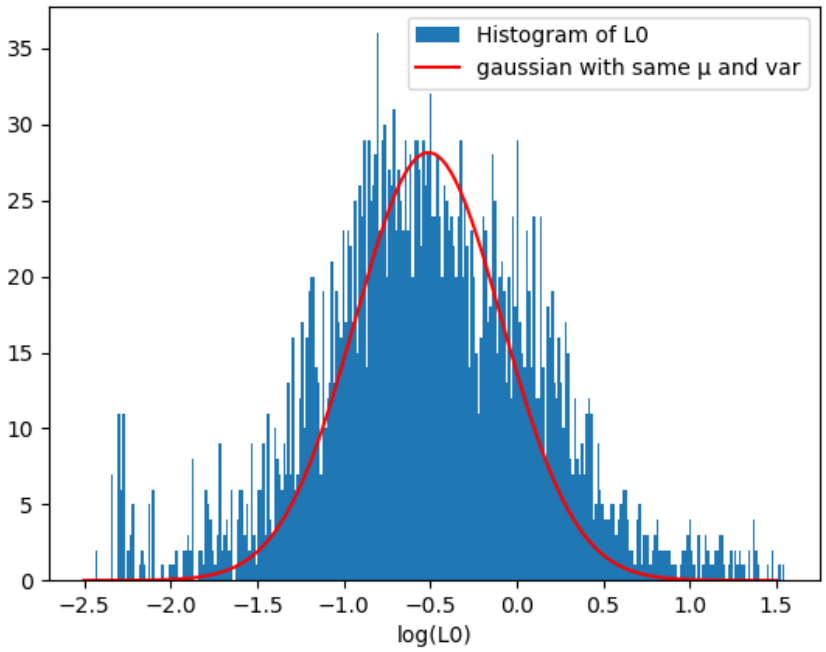

Figure 5.11: Statistical distribution of the "measured" $\log(L_0)$

This chapter has shown that the noise present in the thermosonde measurements has an impact on the performances of all three models but some are more sensitive to that impairment than others. Filtering the data therefore appears to be a mandatory step, it is done here by binning the input data in bins of size B and the statistical study made across the 15 different data sets suggests there is an optimal bin size B_{opt}, even though more sets would be needed to confirm the trend and the value of B_{opt}. Finally, plotting the statistical distribution of the outer scale L_0 shows a bimodal log-normal distribution, the two modes corresponding to the two mean values of L_0 in the troposphere and the stratosphere. From this distribution and setting a confidence interval, one could directly discard outliers during computation. The plot in Figure 5.11 has been obtained with only one data set, it would be interesting in future work to obtain the distribution with a higher number of sets.

Chapter 6

Comparison

This chapter will first present the NWP system WRF as a potential alternative to radiosounding data upon which the models are usually applied to provide an estimation of the refractive index structure constant vertical profile. Then, the performances of the three models will be compared in terms of mean RMSE, RMSE and integrated parameters, to see if one stands out as the absolute best or, most likely, if it depends on the metric of performance used.

6.1 WRF data

"The Weather Research & Forecast (WRF) model is a state of the art mesoscale Numerical Weather Prediction (NWP) system designed for both atmospheric research and operational forecasting applications." [33]. It is a non-hydrostatic model aiming at simulating the state of the atmosphere on a finite domain [11]. This software can produce, among others, idealized cases as well as real measurements-based simulations. The model needs to be specified some inputs to simulate the atmosphere, such as the domain, the type of soil and some meteorological data. These meteorological data are usually coming from reanalysis from measurements[11], such as the ERA5. ERA5 is the fifth generation ECMWF (European Center for Medium-range Weather Forecasts) reanalysis for climate and weather and provides hourly estimates of the atmospheric state with a grid horizontal resolution of $30km$ and vertical resolution of about $600m$ [34, 35].

As the domain becomes larger, the resolution must decrease to keep a total number of grid nodes and therefore the execution time reasonable. However, WRF allows to use *nesting* in order to increase the resolution only in a given sub-domain, i.e. a nested domain. Doing so, only the resolution in a specific region of interest is increased and not for the whole domain. This concept is powerful and allows one to refine the resolution at some region of the domain while keeping the execution time reasonable [11].

The three statistical models studied here need standard meteorological data, usually from balloon flights, to provide an estimated C_n^2 profile. As discussed earlier, those measurements are highly impacted by noise such that raw data are of no use to predict C_n^2 profiles because of the numerical instability of the differential operator in presence of measurement noise and they must be pre-processed. Furthermore, the measurements

might not be available at the precise location of interest or even the desired time. Finally, this method does not provide a good temporal resolution [11].

Therefore, WRF simulated profiles seem to be a convenient alternative since it does not require any sounding material and offers more flexibility concerning the time and location where the profiles are desired. Those profiles are also exempt of measurement noise.

The meteorological profiles needed by the three models have been simulated by WRF at the same location, date and time (roughly) in order to compare the results produced by the models with both sets of input data, i.e. T-REX and WRF. Details about the domain definition from the WRF simulation are summarized in Figure 6.2 and the nested domains are illustrated in Figure 6.1[1]. Such profiles are shown in Figure 6.3. They are

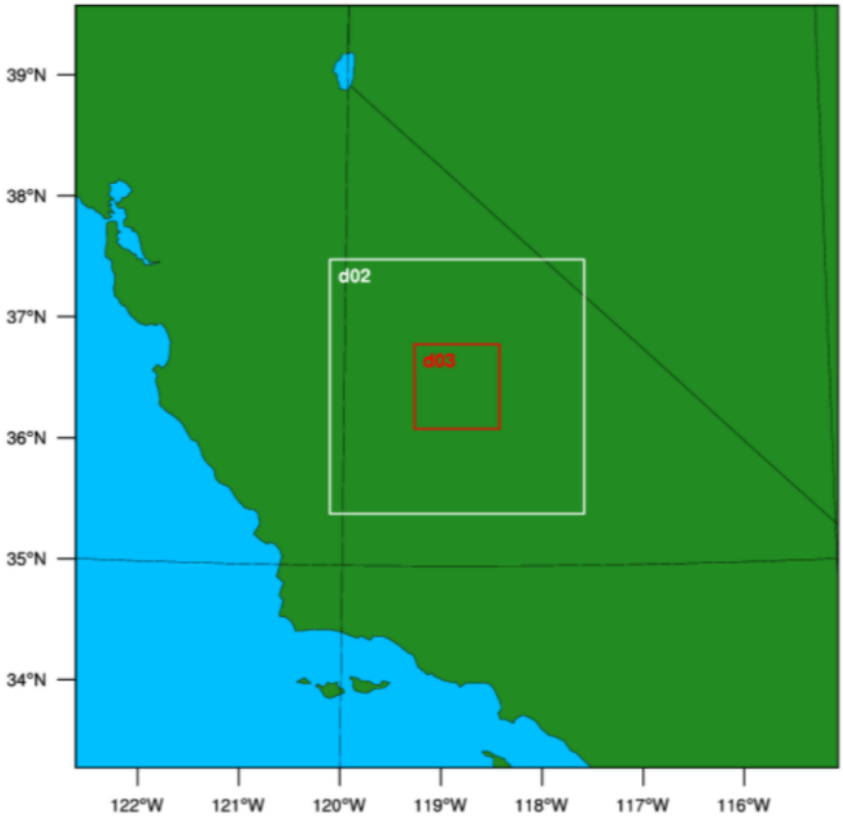

Figure 6.1: Nested domains for the WRF simulation at the T-REX site.

Domain	Grid resolution (km)	Number of grid points	Domain size (km)	Number of vertical levels	Vertical spacing between levels (m)
d01	9	79×79	711×711	250	∼80
d02	3	79×79	237×237	250	∼80
d03	1	79×79	79×79	250	∼80

Figure 6.2: Grid parameters from WRF simulations [36].

clearly smoother than the ones in Figure 5.1, i.e. noise-free. As a consequence of this, the data provided by WRF do not need to be pre-processed before being fed to the models.

[1]This image was provided by Florian Quatresooz

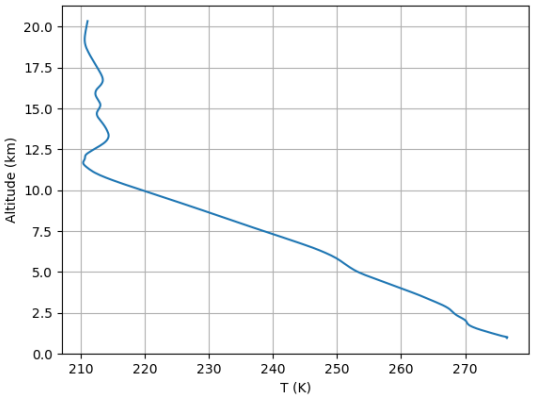

(a) Temperature.

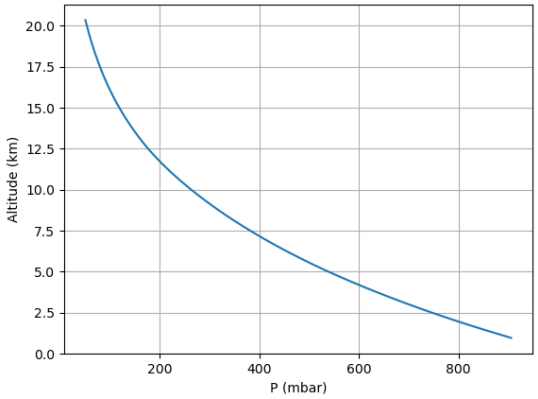

(b) Pressure.

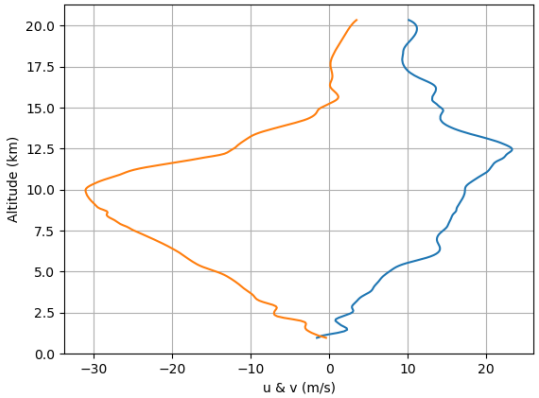

(c) Horizontal wind speed components.

Figure 6.3: Vertical profiles of some atmospheric quantities from WRF simulations.

It appears that WRF is able to reproduce the measured atmospheric profiles with a great accuracy most of the time, when the measurement noise has been effectively removed from the T-REX data. The only divergence relies in the module of the gradient of potential temperature obtained with WRF which sometimes shows extremely small values at low altitude and those are not observed in the T-REX measurements. These extremely low values directly affect the potential refractive index gradient M which is proportional to $\frac{\partial \ln \theta}{\partial h}$. This observation is shown in the graph of M^2 in Figure 6.4 where one can see multiple orders of magnitude differences between the two curves at very specific altitudes (roughly at $1km$ and $6km$). This can induce low-valued outliers in the C_n^2 profiles of models using Tatarskii's formula Equation 4.4 such as Dewan and HMNSP99. In practice however, only HMNSP99 suffers from this behaviour because the $300m$ resolution used by Dewan does not take into account the small-scale variations responsible for the very low values of $\frac{\partial \ln \theta}{\partial h}$ while HMNSP99 uses the resolution of the WRF data, which is of about $80m - 90m$. TV does not show a similar behaviour since it does not rely on Tatarskii's formula. The comparison between the profiles predicted with each of the three models obtained with both WRF simulated data and T-REX measurements is shown in Figure 6.5, the measured C_n^2 is shown as well. The file (*t-rex005.txt*) has been chosen to illustrate the low-valued outliers due to M^2. Apart from this phenomenon, the C_n^2 profiles obtained with both WRF data and T-REX measurements are close one to another as can be seen

in the mean profiles in Figure 6.6, confirming the ability of WRF to accurately simulate atmospheric parameters.

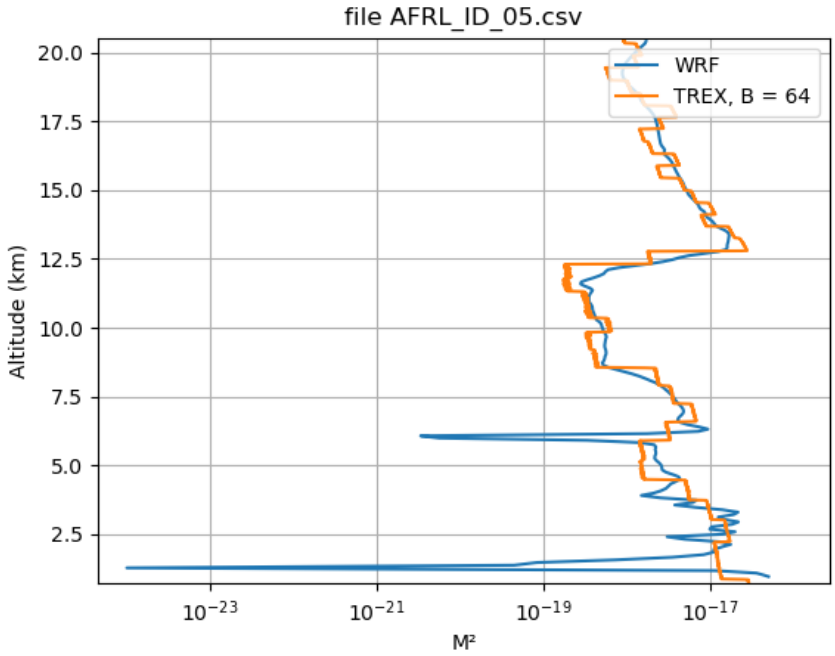

Figure 6.4: Comparison of M^2 obtained with WRF and T-REX data. Measurements were filtered with $B = 64$.

6.2 Performance comparison

In light of the discussions from chapter 5, one would now want to assess the relative performances of each model compared to the others and see, eventually, if one outperforms the others and if so, under what conditions ?

6.2.1 RMSE comparison

The main parameter influencing the the performances of the models is the filtering of the input data, represented by the binning factor B. As a remainder, binning consists in grouping data in bins of B samples and then keeping only the mean value of the bin. Thus higher values of B mean more averaging hence more filtering. Knowing that the average resolution of the T-REX measurement campaign radiosonde data is $\approx 10m$, the bin width in meters can be roughly approximated by $10B$.

The impact of the binning factor on the mean RMSE for all three models is shown in Figure 6.7. As explained before, only a $300m$ resolution has been used for Dewan, following the recommendation of the authors in [27], and the constant value in Figure 6.7 corresponds to the mean RMSE for that particular resolution. It appears TV has a lower mean RMSE than Dewan and HMNSP99 no matter the binning factor while

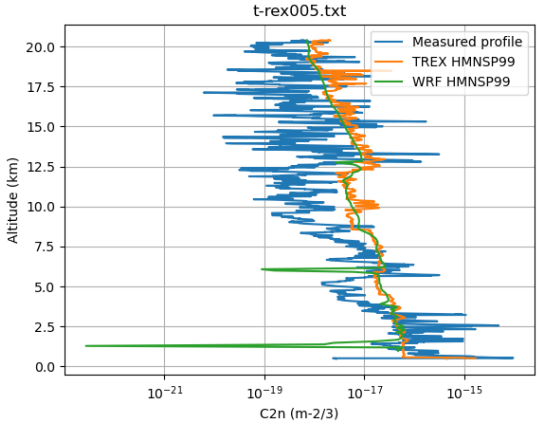

(a) HMNSP99

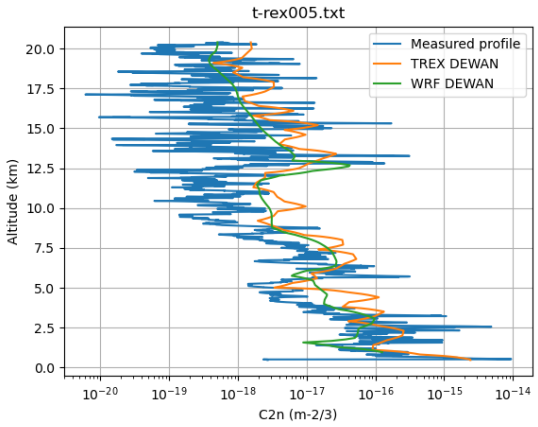

(b) Dewan

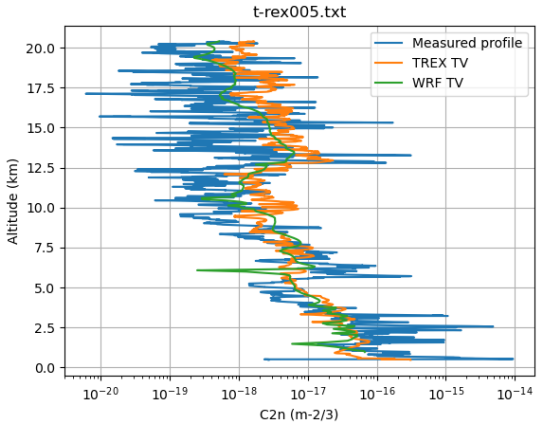

(c) TV

Figure 6.5: Comparison of C_n^2 profiles measured, predicted with the T-REX measurements and with WRF simulated data for the three non-static models.

HMNSP99 strongly suffers from measurement noise and has the worst performances when there is no filtering. Since the optimal performances are obtained with a bin size $B = 64$, from now on all plots shown will correspond to that B unless mentioned otherwise.

HMNSP99 is much more sensitive to filtering than TV because of its mathematical expression ; it has been shown that a numerical gradient amplifies the measurement noise and this gradient appears in an exponential term in the case of HMNSP99. On the other hand, TV is "only" proportional to the square root of the potential temperature gradient and the wind shear, such that the error will be less amplified.

Based on this metric of performance, it is possible to rank the models in ascending order of performance : Dewan $<$ HMNSP99 $<$ TV. However, it is not wise to compare these models only on the basis of a scalar metric of performance knowing that the complete altitude profile of the RMSE is far from being constant, as shown in Figure 6.8a. The figure shows that, even if TV seems to be superior to the other two, it is difficult to proclaim one model as the best for the whole altitude range considered. Furthermore, Figure 6.8b suggests that Dewan provides a better estimation of the C_n^2 *mean* vertical

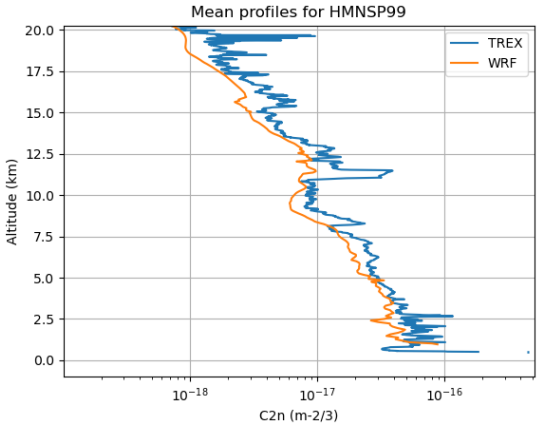

(a) HMNSP99

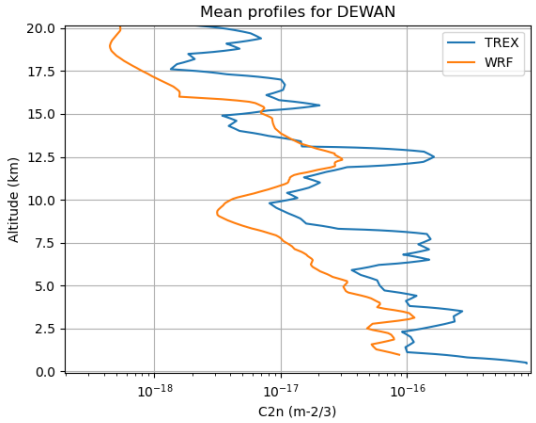

(b) Dewan

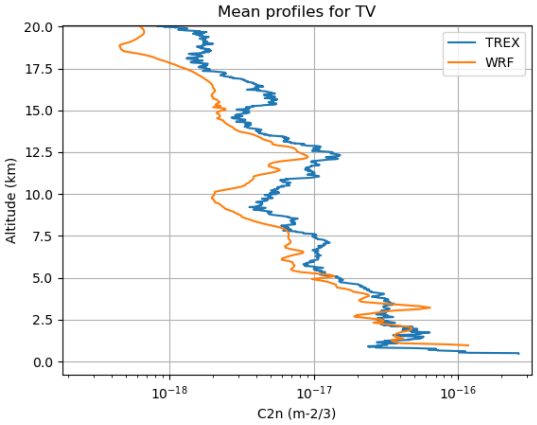

(c) TV

Figure 6.6: Comparison of the mean C_n^2 profiles obtained both with T-REX measurements and WRF simulated data.

profile, which seems to invalidate the previous observations. This peculiar behaviour can be explained if one remembers that the C_n^2 varies over multiple orders of magnitude from one altitude to another and from one day to another. Hence, if one data set was obtained under very poor conditions (large C_n^2) compared to the others, the mean profile will be very close to this particular profile. It is in fact what happened here, i.e. one of the T-REX files (file 12) contains a C_n^2 profile that is much larger than the others (by a factor of about 100). Moreover, it appeared that Dewan performed better than the other two models for that particular file, hence the better agreement between Dewan and the mean measured C_n^2 profile. This observation is illustrated in Figure 6.9. Therefore it is not as straight forward as one would think to extract conclusions about the performances of a model and it is crucial to use metrics rather than judging by the look of the mean profile.

6.2.2 Integrated parameters comparison

Because it is difficult to clearly identify one model as the best for the whole altitude range considered, one could also compare them according to a more local criterion. To that

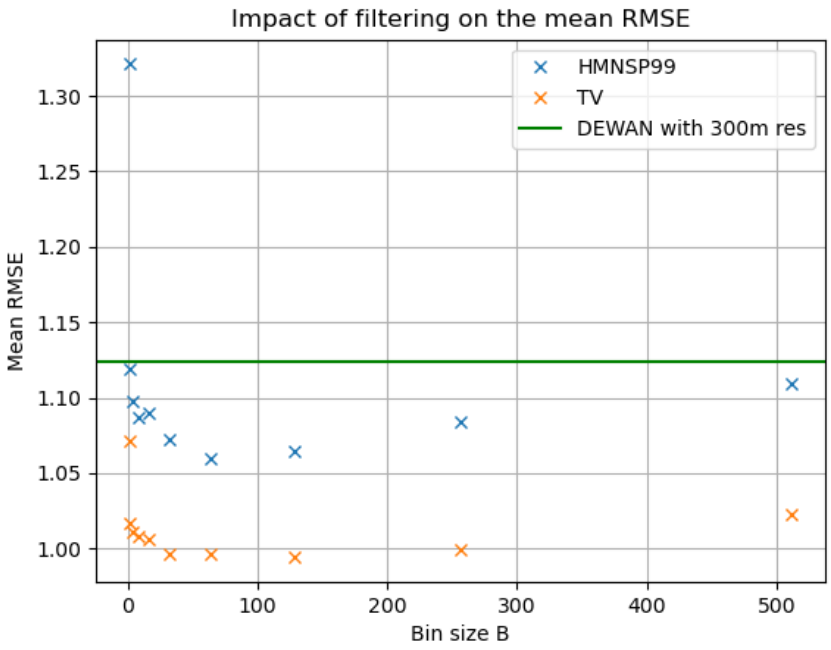

Figure 6.7: Comparison of the mean RMSE as a function of B for all 3 models.

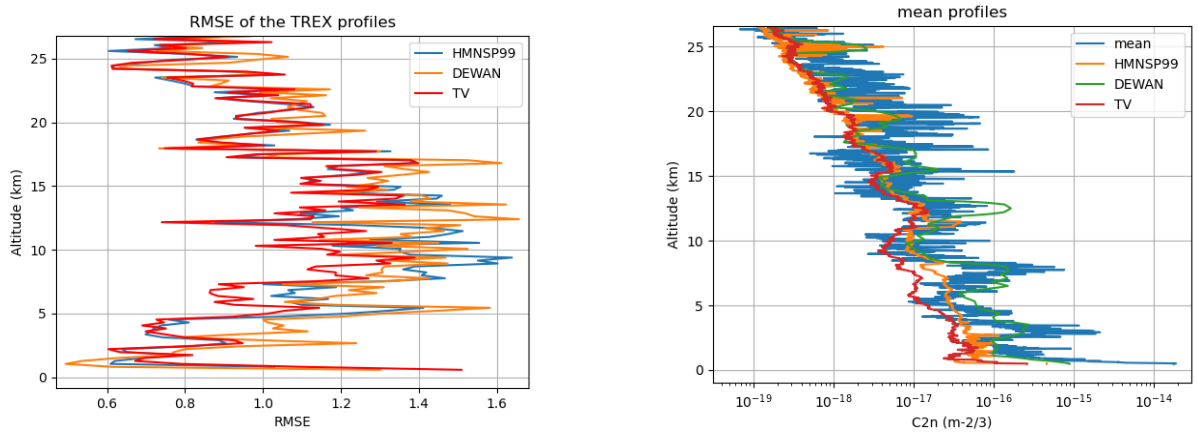

(a) RMSE

(b) Mean profiles

Figure 6.8: RMSE and mean profiles of the 3 models applied to the T-REX data

end, the coherence length r_0 and the isoplanatic angle θ_0 are extracted from the $C_n^2(h)$ profiles obtained with the T-REX data and compared to the ones obtained from the measured profiles. Indeed, these two integrated parameters are sensitive to the turbulence in different regions of the atmosphere and therefore might provide a scalar metric of performance for more localized layers.

Fried's parameter r_0

Fried's parameter (or equivalently the coherence length) r_0 is obtained from the $C_n^2(h)$ profile according to Equation 3.1. Because the refractive index structure constant rapidly

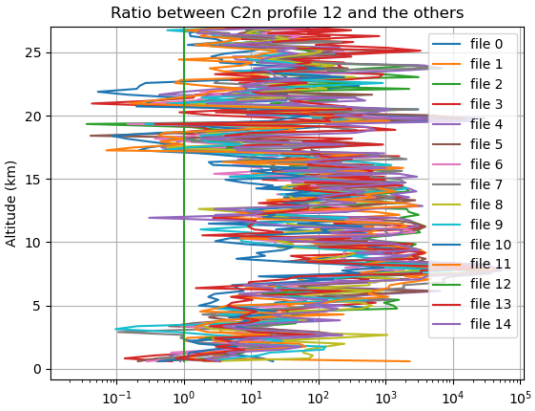

(a) Amplitude comparison between the profile from file 12 and the others

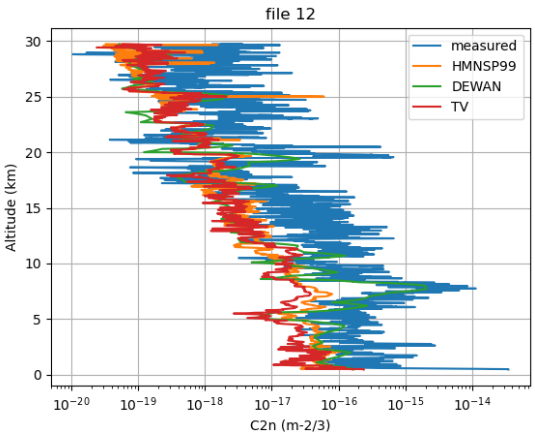

(b) $C_n^2(h)$ profile from T-REX file 12

Figure 6.9: Impact of poor conditions on the mean C_n^2 profile

decreases with altitude, r_0 is very sensitive to the boundary layer, i.e. the part of the atmosphere closest to the ground. Let us investigate the rate at which the coherence length reaches its final value, to do so one defines the *intermediate coherence length* r (supposing a vertical path) as :

$$r(h) = \left(0.423k^2 \int_{h_0}^{h} C_n^2(h')dh'\right)^{-3/5} \tag{6.1}$$

The evolution of $r(h)$ as a function of the altitude h shows that the intermediate coherence length reaches its final value r_0 at a certain rate, depending on the vertical structure of the turbulence. High altitude turbulent layers are responsible for lower rates. This is shown in four different cases in Figure 6.10, the red line corresponds to the threshold altitude h_{th} such that $\frac{r_0}{r(h_{th})} = 0.9$. The average threshold altitude $h_{th,av} = 4km$ confirms that the coherence length r_0 (or equivalently the seeing ϵ_0) is mostly determined by the boundary layer.

Now the coherence length has been computed from the profiles estimated with the three models applied to the T-REX data and compared to the values obtained with the measured profiles. This is shown in Figure 6.14a. The results in terms of mean coherence length $\bar{r_0}$ and RMSE are summarized in Table 6.1. It is clear from this point of view that Dewan performs better than the other two models. The mean coherence length estimated by Dewan is much closer to the measured one and the RMSE is the lowest among the three. The fact that all three models have higher values of r_0 than the measured one most of the time (most of the points in Figure 6.14a are above the blue line) means that they underestimate the turbulence profile at least in the lower parts of the atmosphere. However this is much more the case for TV and HMNSP99 than for Dewan since they give much higher values of r_0.

These results confirm the initial idea that it is difficult to present one model as the best since their performances depend on the altitude and some might be more suited for a certain

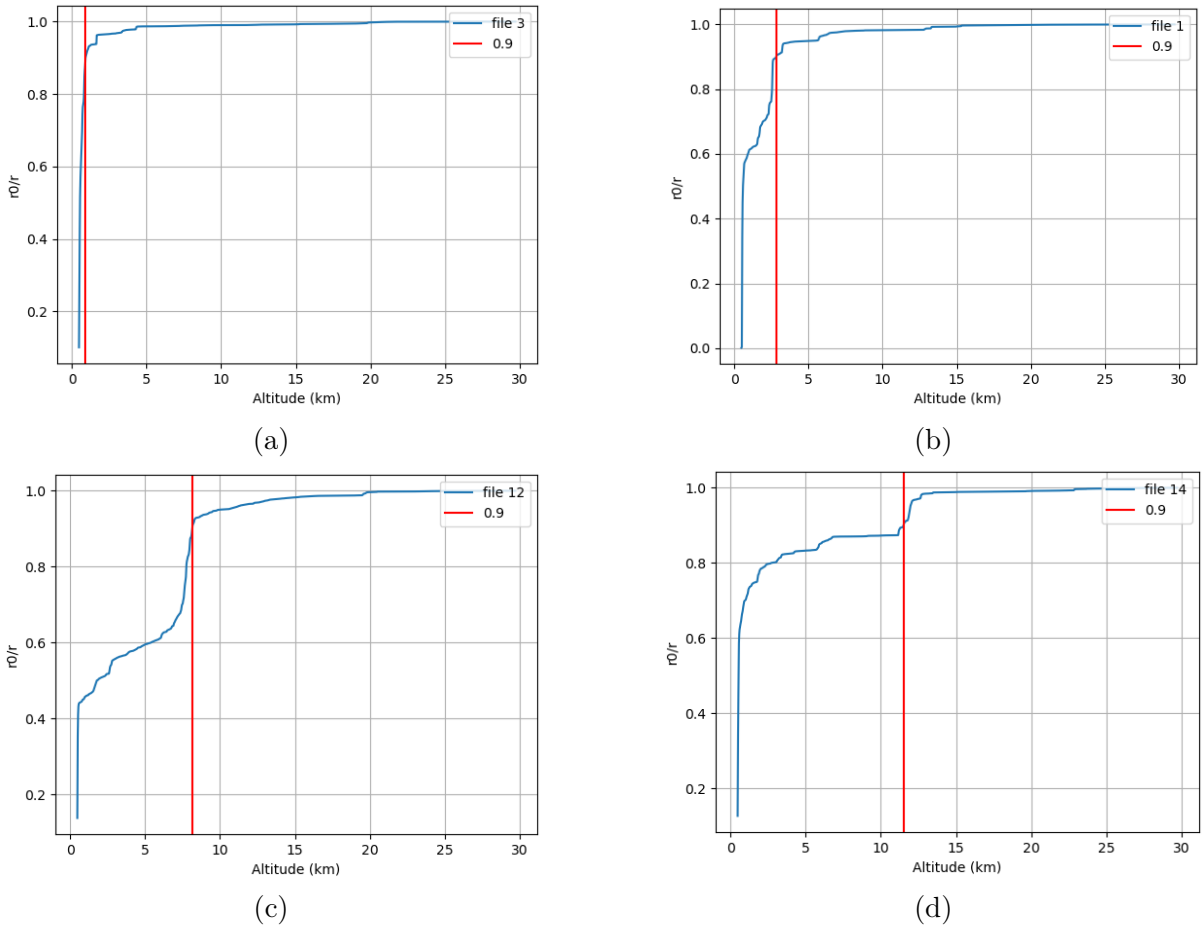

Figure 6.10: Evolution of the ratio $\frac{r_0}{r(h)}$ as a function of the altitude for 4 different T-REX files. The vertical red line shows h_{th}.

	HMNSP99	Dewan	TV	Measured
$\bar{r_0}$ (cm)	13.885	7.069	17.933	5.211
RMSE (cm)	9.176	3.63	13.151	/

Table 6.1: Comparison of the r_0 estimated with the three models. The mean measured r_0 is added as reference.

atmospheric layer than others. Dewan seems to be more capable in estimating Fried's parameter than TV and HMNSP99 and therefore, seems more accurate in reconstructing the C_n^2 profile, on average, in the lower parts of the atmosphere (within the first $4km$). A representative sample of the C_n^2 profiles zoomed on the region from ground up to $5km$ is shown in Figure 6.11, illustrating the better agreement between Dewan and the measured profiles most of the time in the boundary layer.

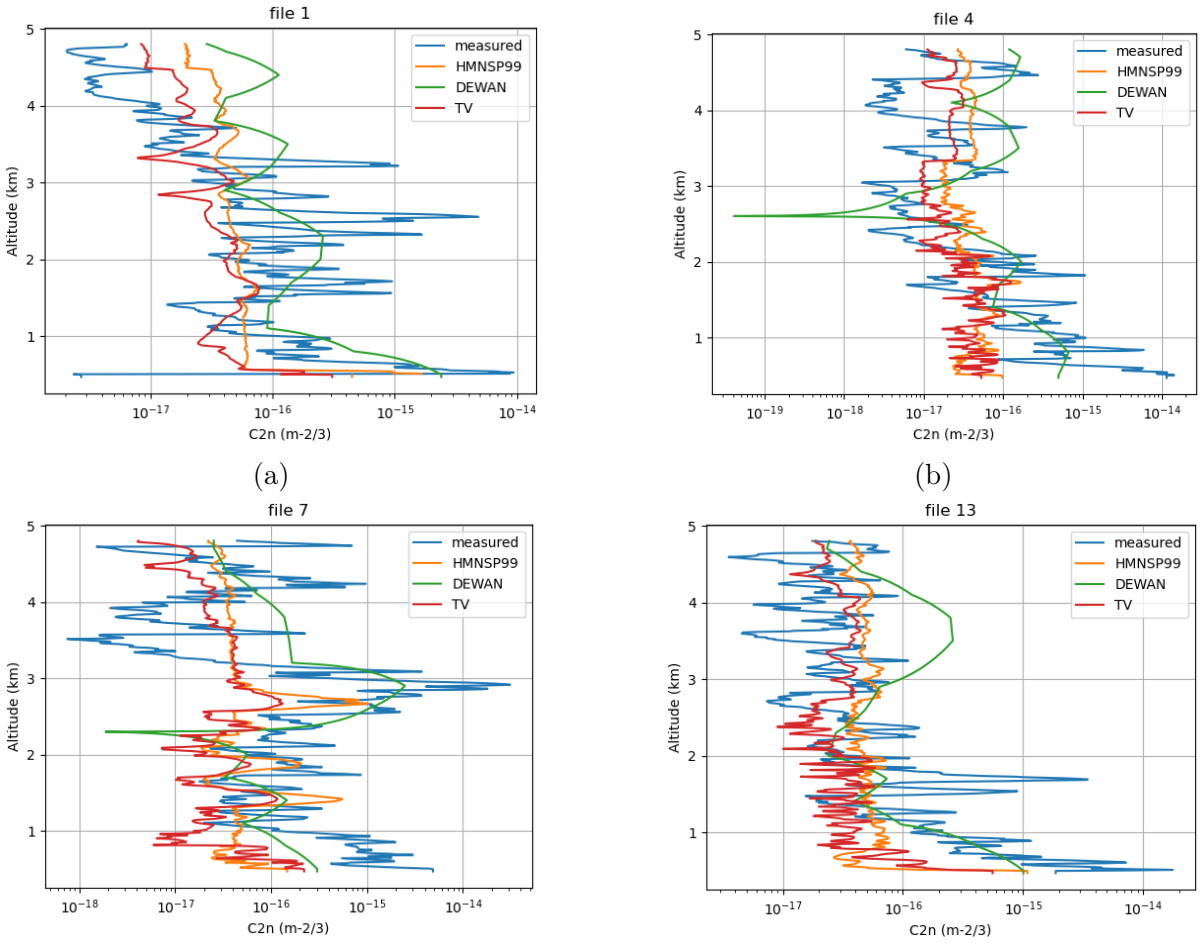

Figure 6.11: C_n^2 profiles zoomed from ground up to $5km$. Dewan is often closer to the measured profile, hence a better estimation of r_0.

Isoplanatic angle

With a approach similar to that of the coherence length, one can define the *intermediate isoplanatic angle* θ (supposing a vertical path) as :

$$\theta(h) = \left(2.91k^2 \int_{h_0}^{h} C_n^2(h')h'^{5/3}dh'\right)^{-3/5} \tag{6.2}$$

Because of the weighing function $h'^{5/3}$, the isoplanatic angle is not so sensitive to low altitude turbulent layers but rather some high altitude ones. This means that the final value θ_0 is reached at a lower rate than for the r_0, i.e. at higher altitudes. The evolution of $\theta(h)$ is shown in Figure 6.12, the red lines encapsulate the altitude range within which 90% of the final value of the isoplanatic angle is reached. The mean values of $h_{th,1}$ and $h_{th,2}$ are $0.65km$ and $20km$ respectively. Figure 6.12 shows that, unlike r_0, θ_0 is not very sensitive to the boundary layer and usually $\theta(h)$ has a step increase caused by higher altitude turbulent layers such as the one often encountered at the tropopause ($\approx 12km$) as in Figure 6.12a and Figure 6.12c. It is the ability of the models to accurately estimate

the altitude and the amplitude of the turbulent layers above the boundary layer that will dictate their performances in estimating the isoplanatic angle.

The comparison between the estimated and measured isoplanatic angles is shown in Figure 6.14b and the results in terms of mean isoplanatic angle $\bar{\theta_0}$ and RMSE are summarized in Table 6.2. From these results it appears that Dewan and HMNSP99 provide in general a better estimation of θ_0 (with Dewan being slightly superior) than TV ; $\bar{\theta_0}$ is closer to the measured value and lower RMSE. HMNSP99 and TV still tend to overestimate θ_0 (i.e. underestimate C_n^2 profiles) while Dewan gives underestimated values of θ_0 (overestimated C_n^2 profiles) more than half of the time. This suggests that Dewan is able to estimate more accurately the altitude and amplitude of the turbulent layers. Figure 6.13 shows 4 different profiles where Dewan provides a better estimation of the altitude and amplitude of the turbulent layers.

	HMNSP99	Dewan	TV	Measured
$\bar{\theta_0}$ (μrad)	6.658	3.857	8.309	4.968
RMSE (μrad)	2.521	2.256	3.724	/

Table 6.2: Comparison of the θ_0 estimated with the three models. The mean measured θ_0 is added as reference.

This chapter first presented the Numerical Weather Forecast system WRF and showed that it is able to accurately reconstruct the vertical profiles of standard meteorological parameters such as the temperature, pressure and windspeed. To do so WRF needs a terrain model and meteorological reanalysis data (e.g. ERA5 data) which are available online and span the planet with a horizontal and vertical grid resolution of $30km$ and $600m$ respectively, every hour. This is very interesting if no meteorological station with balloon data are available around a location of interest to provide the input data to the models.

Then the comparison between the performances of the different models according to multiple metrics highlighted that it is difficult to proclaim one model as the absolute best. Indeed, the mean RMSE suggests that TV performs better than HMNSP99 which performs better than Dewan. This test also stressed the impact of filtering on the performances of the models relative one to another. The total altitude profiles of the RMSE curves suggest again that TV has the best performances from above the boundary layer up to $16km$, the difference between HMNSP99 and Dewan is less evident and both models seem roughly equivalent.

Finally, the estimated and measured integrated parameters r_0 and θ_0 have been compared and the results suggested another ranking of the models with Dewan being superior to the other two and TV presenting the lowest performances with the highest RMSE. Therefore it appears that Dewan provides a better estimation of the turbulence in the boundary layer as well as the altitude and amplitude of turbulent layers. However, TV has globally a lower RMSE meaning that it is usually closer to the measured profile but the integrated parameters depend highly on the strong turbulent layers. All the individual C_n^2 profiles are available at the end of this master thesis, in Appendix A.

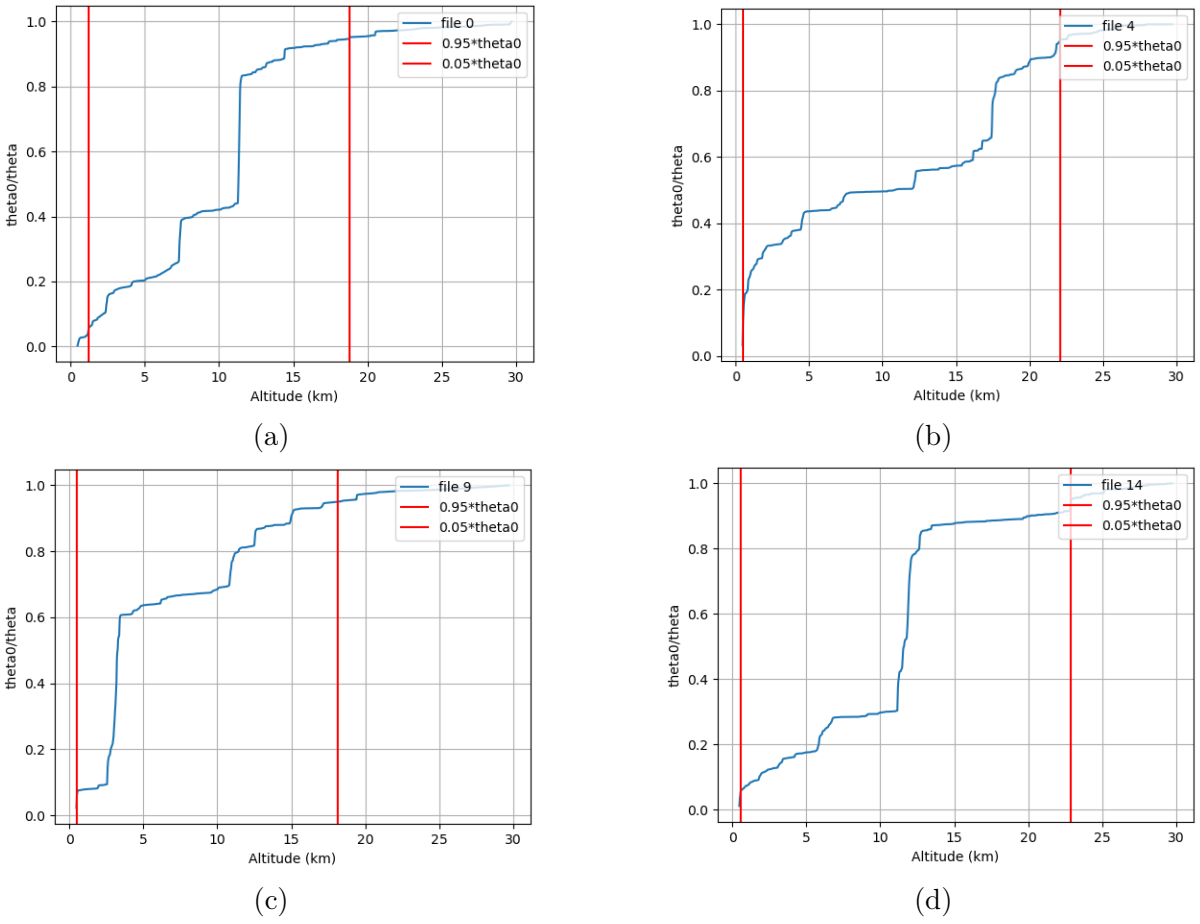

Figure 6.12: Evolution of the ratio $\frac{\theta_0}{\theta(h)}$ as a function of the altitude for 4 different T-REX files. The vertical red lines show $h_{th,1}$ and $h_{th,2}$.

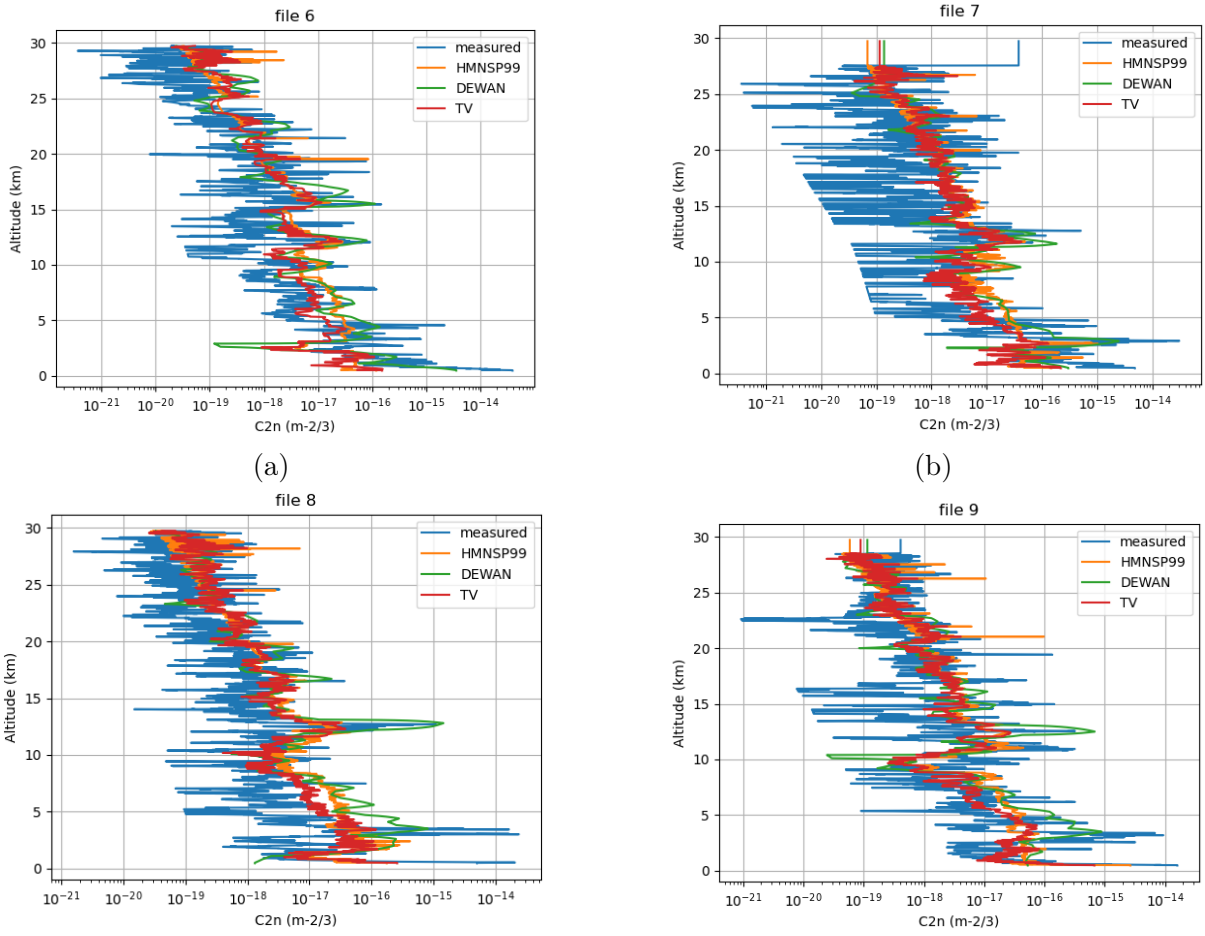

Figure 6.13: Dewan provides better estimations than TV and HMNSP99 of the altitude and amplitude of the turbulent layers.

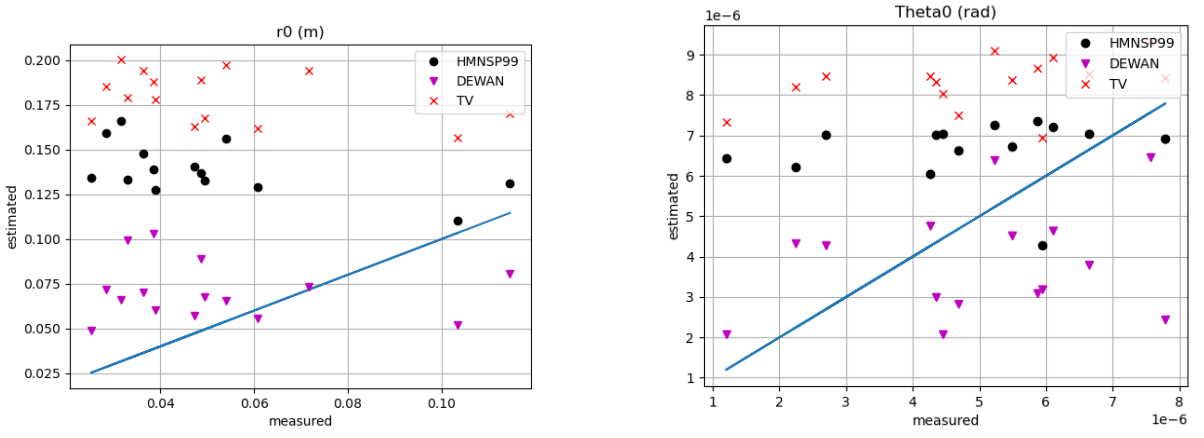

(a) Fried's parameter

(b) Isoplanatic angle

Figure 6.14: Comparison of the integrated parameters estimated with the three models.

Chapter 7

Application to the ground station in Redu (Belgium)

Redu is a potential site for an optical ground terminal, located in the South of Belgium. Therefore optical turbulence, and more precisely, seeing characterization is of primary importance. Unlike most of the astronomical sites, Redu is at a low altitude (i.e. $350m$) and is expected to feature major degradation due to the boundary layer turbulence [36]. Seeing measurements were recorded during two nights in February and one in September 2019 and discussed in [36]. They were also made available such that they could be used for comparison with the seeing estimated with the three models discussed in this work.

7.1 The measurements

The seeing was measured with a differential image motion monitor (DIMM) during the nights of the 5^{th} and 14^{th} February and the 9^{th} September 2019. The instrument produces a seeing value every 5 to 10 seconds, those measurements being noisy they are binned in bins of 5 minutes (30 to 60 samples per bin) before comparing with the estimated values [36].

7.2 Results and discussion

In order to obtain estimated values of the seeing, vertical profiles of the temperature, pressure and wind speed are generated with WRF in a similar manner as described in section 6.1. Those data are used as input to the three models (TV, HMNSP99 and Dewan) and the seeing is then extracted from the resulting C_n^2 profile. This procedure is repeated in order to provide a seeing estimation every 5 minutes during the corresponding measurement nights. The comparison between measurements and estimations of the seeing is shown for the three nights in Figure 7.1. Because each estimation requires a C_n^2 profile, only the last one is shown for every night, i.e. the C_n^2 profile corresponding to the last seeing point (the rightmost).

The results show that the three models tend to underestimate the seeing, meaning that they underestimate the refractive index structure constant in the lower parts of the

atmosphere (at least !). Here again it appears that Dewan provides a better estimation of the seeing and therefore of the boundary layer, which is responsible for most of the seeing, as explained before. Indeed, the authors in [36] showed that the seeing at Redu is mainly determined by the first $500m$ above the ground.

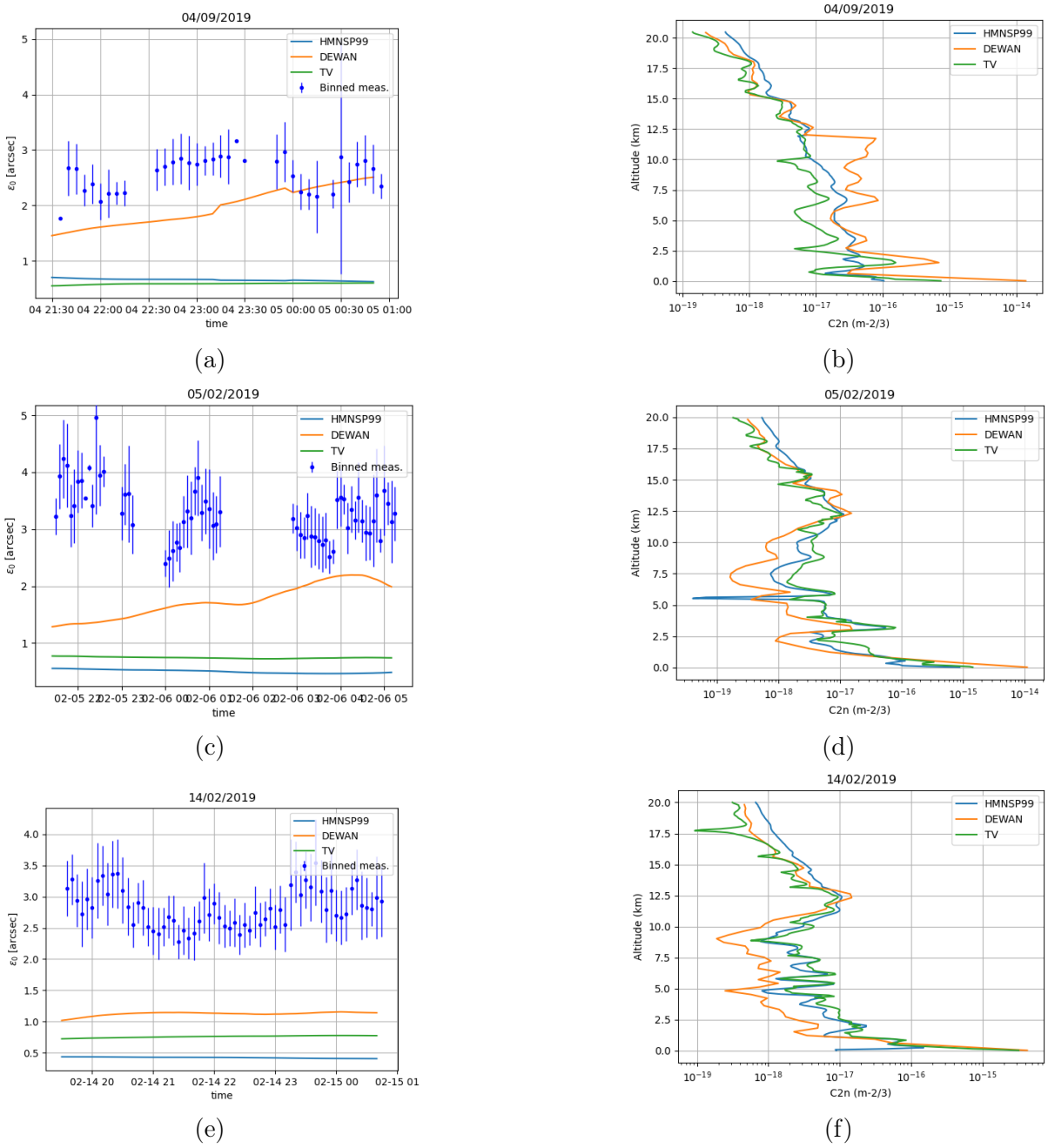

Figure 7.1: Comparison between the measured and estimated seeing every 5 minutes during the three measurement nights at Redu (on the left). The estimated C_n^2 profiles for the last data point is shown on the right.

Chapter 8

Conclusion

8.1 Take-away messages

This master thesis presents the mathematical and physical framework within which optical turbulence is described, along with the main characterization tools and representative parameters. It also provides a representative set of estimation models of various levels of complexity, from the static ones such as the $HV_{5/7}$ to the numerical ones such as Meso-NH. This review of the literature allows one to get a grasp on the subject and was the firs objective of this work.

The second objective was to perform an in-depth study of three statistical models, chosen for the good trade-off they offer between complexity and performance. The T-REX measurement campaign provided 15 different data files to assess the performances of the different models according to the RMSE and the extracted integrated parameters. The study showed that the models are sensitive to the vertical resolution of the data and also to the measurement noise, mostly the two models using Tatarskii's relation Equation 4.4. Radiosounding provides data with the finest resolution but also records a substantial noise which must be removed before obtaining the C_n^2. It appeared that TV had on average the lowest RMSE however Dewan provides the best estimations of the isoplanatic angle and the coherence length, due to its better reconstruction of the boundary layer as well as the amplitude and altitude of the high altitude turbulence peaks. Therefore the performance assessment depends on the metric used.

8.2 To go further

One way to go further in the study of C_n^2 modelling would naturally to investigate the numerical models as they provide the most accurate results as well as insight on the physics of the turbulence.

Another interesting path would be to consider more advanced statistical models, able to increase their performances while maintaining a low complexity. Such advanced models could be inspired from the WSTG model from [19] which have fitting coefficients depending not only on the altitude but also the joint values of the wind shear and the temperature

gradient.

Appendix A

Individual profiles

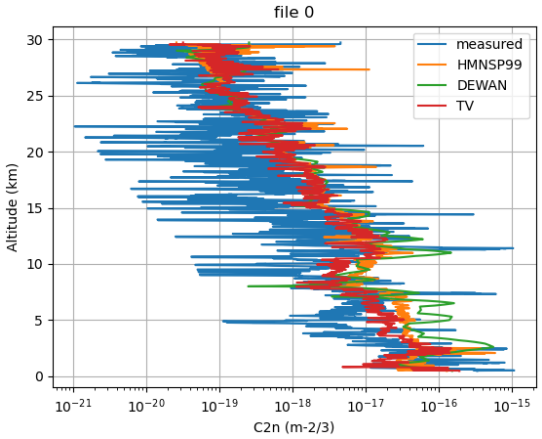
file 0
measured
HMNSP99
DEWAN
TV
Altitude (km)
C2n (m-2/3)

(a)

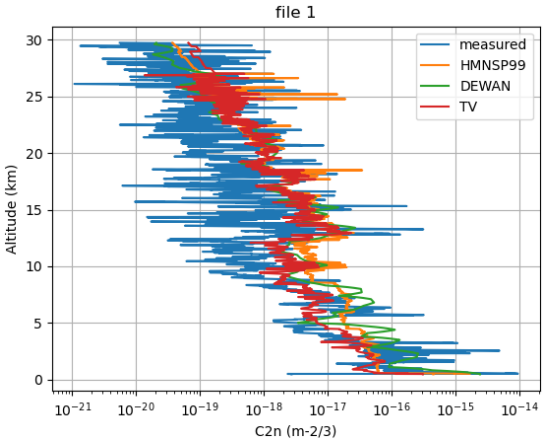
file 1
measured
HMNSP99
DEWAN
TV
Altitude (km)
C2n (m-2/3)

(b)

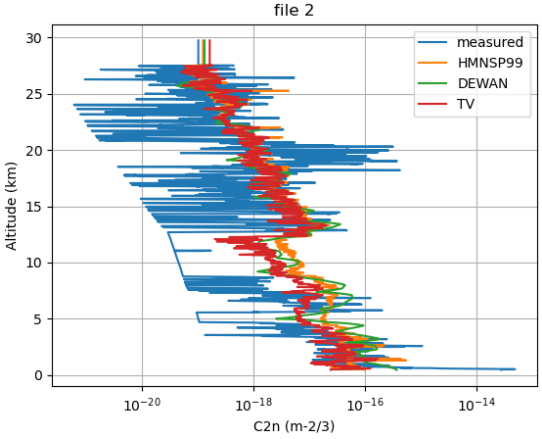
file 2
measured
HMNSP99
DEWAN
TV
Altitude (km)
C2n (m-2/3)

(c)

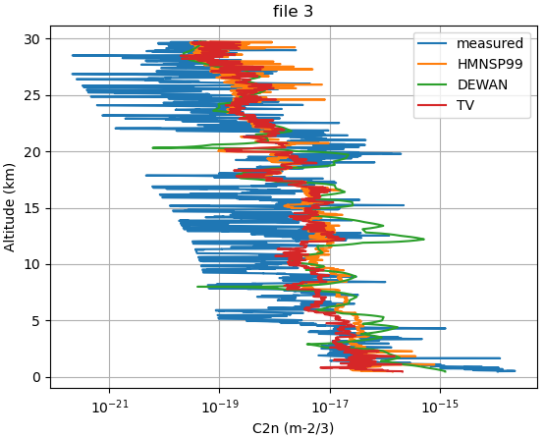
file 3
measured
HMNSP99
DEWAN
TV
Altitude (km)
C2n (m-2/3)

(d)

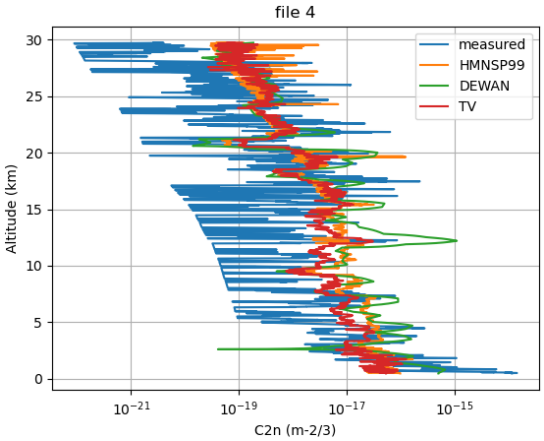
file 4
measured
HMNSP99
DEWAN
TV
Altitude (km)
C2n (m-2/3)

(e)

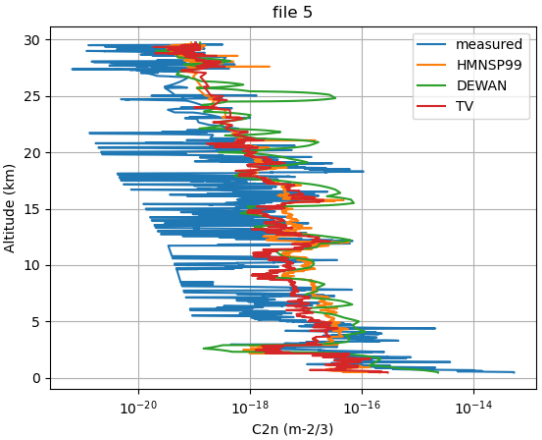
file 5
measured
HMNSP99
DEWAN
TV
Altitude (km)
C2n (m-2/3)

(f)

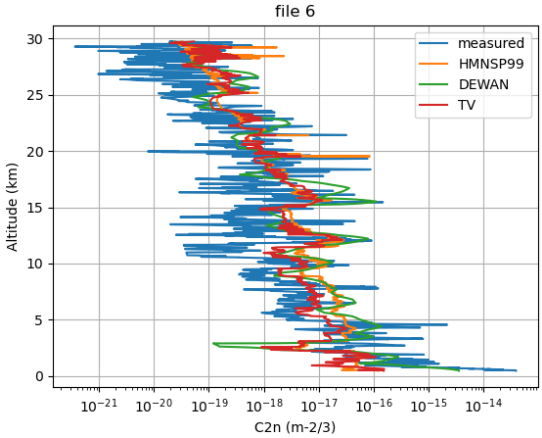
file 6
measured
HMNSP99
DEWAN
TV
Altitude (km)
C2n (m-2/3)

(g)

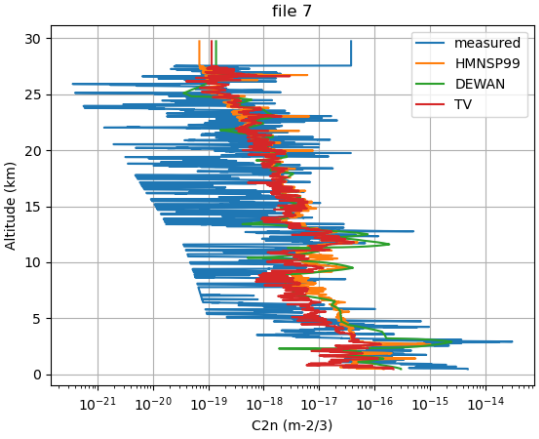
file 7
measured
HMNSP99
DEWAN
TV
Altitude (km)
C2n (m-2/3)

(h)

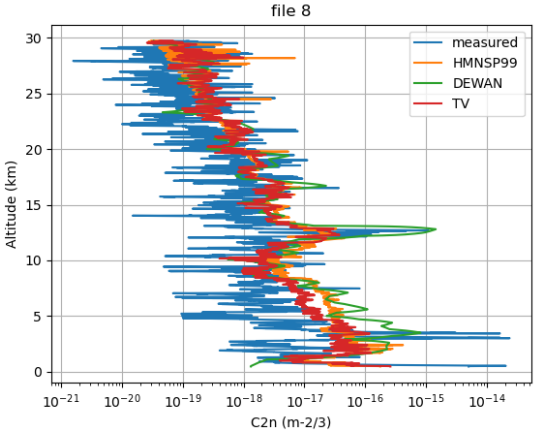
file 8
measured
HMNSP99
DEWAN
TV
Altitude (km)
C2n (m-2/3)

(i)

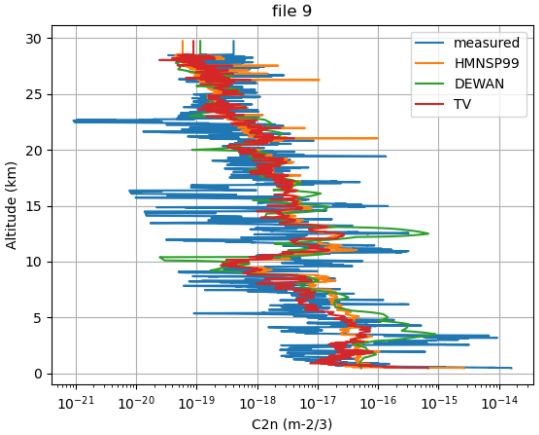
file 9
measured
HMNSP99
DEWAN
TV
Altitude (km)
C2n (m-2/3)

(j)

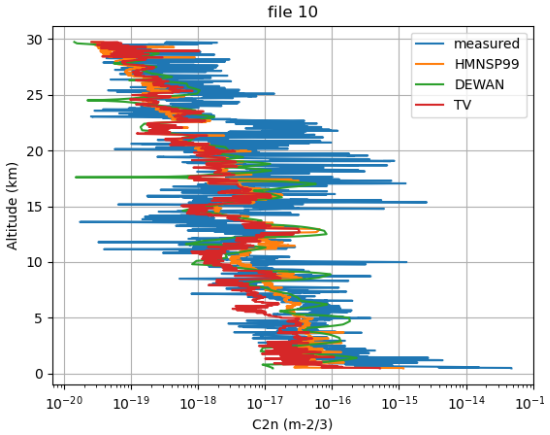
file 10
measured
HMNSP99
DEWAN
TV
Altitude (km)
C2n (m-2/3)

(k)

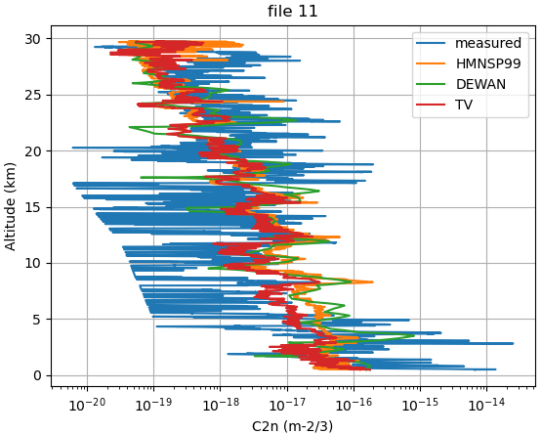
file 11
measured
HMNSP99
DEWAN
TV
Altitude (km)
C2n (m-2/3)

(l)

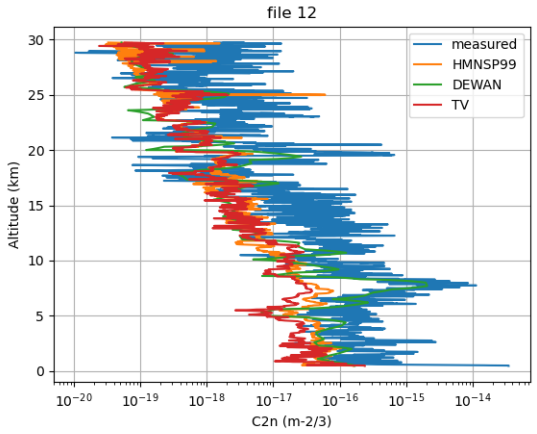

(m)

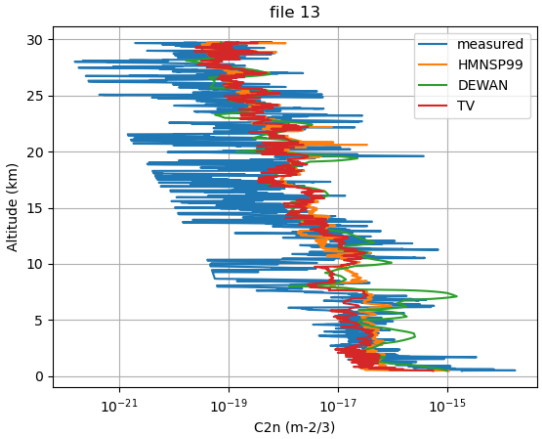

(n)

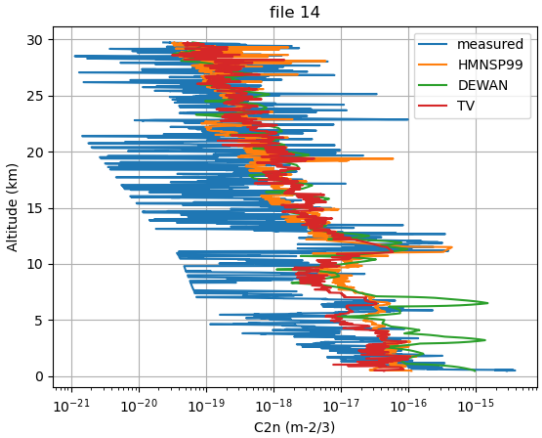

(o)

Figure A.1: Individual estimated and measured $C_n^2(h)$ profiles of the 15 T-REX data files.

Bibliography

[1] J. Mohr, R. Johnston, and P. Cottrell, "Optical turbulence measurements and models for mount john university observatory," Publications of the Astronomical Society of Australia, vol. 27, 08 2010.

[2] A. Ishimaru, Multiple Scattering, Turbulence, Rough Surfaces, and Remote Sensing. Academic Press, 1978.

[3] L. C. Andrews and R. L. Phillips, Laser Beam Propagation through Random Media. SPIE—The International Society for Optical Engineering, 2005.

[4] J. Vernin, "Mechanism of formation of optical turbulence (Invited Speaker)," in Astronomical Site Evaluation in the Visible and Radio Range, ser. Astronomical Society of the Pacific Conference Series, J. Vernin, Z. Benkhaldoun, and C. Muñoz-Tuñón, Eds., vol. 266, Jan. 2002, p. 2.

[5] A. D. Wheelon, Electromagnetic scintillation 1. Geometrical optics. Cambridge University Press, 2001.

[6] Citizendium, "Gaussian units — citizendium,," 2021, [Online; accessed 29-September-2022]. [Online]. Available: https://citizendium.org/wiki/index.php?title=Gaussian_units&oldid=505701

[7] A. D. Wheelon, Electromagnetic scintillation 2. Weak scattering. Cambridge University Press, 2003.

[8] Wikipedia contributors, "Green's function — Wikipedia, the free encyclopedia," 2022, [Online; accessed 3-October-2022]. [Online]. Available: https://en.wikipedia.org/w/index.php?title=Green%27s_function&oldid=1107283486

[9] C. Bi, X. Qian, Q. Liu, W. Zhu, X. Li, T. Luo, X. Wu, and C. Qing, "Estimating and measurement of atmospheric optical turbulence accordingto balloon-borne radiosonde for three sites in china," J. Opt. Soc. Am. A, vol. 37, no. 11, pp. 1785–1794, Nov 2020. [Online]. Available: http://opg.optica.org/josaa/abstract.cfm?URI=josaa-37-11-1785

[10] H. Kaushal and G. Kaddoum, "Free space optical communication: Challenges and mitigation techniques," 2015. [Online]. Available: https://arxiv.org/abs/1506.04836

[11] C. Giordano, "Prediction et optimisation des techniques pour l'observation à haute resolution angulaire et pour la future generation de très grands telescopes," Theses, Université Nice Sophia Antipolis, Dec. 2014. [Online]. Available: https://tel.archives-ouvertes.fr/tel-01144348

[12] "Astronomical seeing - Wikipedia — en.wikipedia.org," https://en.wikipedia.org/wiki/Astronomical_seeing, [Accessed 28-Dec-2022].

[13] "vik dhillon: phy217 - adaptive optics — vikdhillon.staff.shef.ac.uk," http://www.vikdhillon.staff.shef.ac.uk/teaching/phy217/telescopes/phy217_tel_adaptive.html, [Accessed 28-Dec-2022].

[14] M. Azouit and J. Vernin, "Optical turbulence profiling with balloons relevant to astronomy and atmospheric physics," Publications of the Astronomical Society of the Pacific, vol. 117, pp. 536–543, 04 2005.

[15] ——, "Remote investigation of tropospheric turbulence by two-dimensional analysis of stellar scintillation," Journal of Atmospheric Sciences, vol. 37, no. 7, pp. 1550 – 1557, 1980. [Online]. Available: https://journals.ametsoc.org/view/journals/atsc/37/7/1520-0469_1980_037_1550_riottb_2_0_co_2.xml

[16] M. Sarazin and F. Roddier, "The ESO differential image motion monitor," , vol. 227, no. 1, pp. 294–300, Jan. 1990.

[17] A. A. Tokovinin, "A new method of measuring atmospheric seeing," Astronomy Letters, vol. 24, no. 5, pp. 662–664, Sep. 1998.

[18] R. Lyman, T. Cherubini, and S. Businger, "Forecasting seeing for the Maunakea Observatories," Monthly Notices of the Royal Astronomical Society, vol. 496, no. 4, pp. 4734–4748, 06 2020. [Online]. Available: https://doi.org/10.1093/mnras/staa1787

[19] M. Xu, S. Shao, N. Weng, and Q. Liu, "Analysis of the optical turbulence model using meteorological data," Remote Sensing, vol. 14, no. 13, 2022. [Online]. Available: https://www.mdpi.com/2072-4292/14/13/3085

[20] L. Gravley, S. Fiorino, R. Bartell, G. Perram, M. Krizo, and K. Le, "Comparison of climatological optical turbulence profiles to standard, statistical, and numerical models using heleeos," Journal of Directed Energy, vol. 2, p. 347, 07 2007.

[21] D. Sprung, C. Ullwer, A. M. J. van Eijk, and K. Stein, "Investigation of vertical profiles of optical turbulence from mesoscale simulations runs and radiosonde data," in Environmental Effects on Light Propagation and Adaptive Systems IV, ser. Society of Photo-Optical Instrumentation Engineers (SPIE) Conference Series, K. Stein and S. Gladysz, Eds., vol. 11860, Sep. 2021, p. 1186008.

[22] L. F. Otoniel Canuet, "Atmospheric turbulence profile modeling for satellite-ground laser communication," Ph.D. dissertation, UPC, Escola d'Enginyeria de Telecomunicació i Aeroespacial de Castelldefels, Jul 2015. [Online]. Available: http://hdl.handle.net/2117/86039

[23] H. Trinquet and J. Vernin, "A model to forecast seeing and estimate c2n profiles from meteorological data," Publications of the Astronomical Society of the Pacific, vol. 118, no. 843, p. 756, may 2006. [Online]. Available: https://dx.doi.org/10.1086/503165

[24] Abahamid, A., Jabiri, A., Vernin, J., Benkhaldoun, Z., Azouit, M., and Agabi, A., "Optical turbulence modeling in the boundary layer and free atmosphere using instrumented meteorological balloons," A&A, vol. 416, no. 3, pp. 1193–1200, 2004. [Online]. Available: https://doi.org/10.1051/0004-6361:20031390

[25] Masciadri, E., Vernin, J., and Bougeault, P., "3d mapping of optical turbulence using an atmospheric numerical model - i. a useful tool for the ground-based astronomy," Astron. Astrophys. Suppl. Ser., vol. 137, no. 1, pp. 185–202, 1999. [Online]. Available: https://doi.org/10.1051/aas:1999474

[26] H. Trinquet and J. Vernin, "A statistical model to forecast the profile of the index structure constant

$$C_N^2,'' \underline{Environmental Fluid Mechanics}, vol.\ 7, pp.397 - -407, 102007.$$

[27] E. M. Dewan, A Model for C2n (optical turbulence) profiles using radiosonde data. Directorate of Geophysics, Air Force Materiel Command, 1993, no. 1121.

[28] S. Wu, X. Wu, C. Su, Q. Yang, J. Xu, T. Luo, C. Huang, and C. Qing, "Reliable model to estimate the profile of the refractive index structure parameter (cn2) and integrated astroclimatic parameters in the atmosphere," Opt. Express, vol. 29, no. 8, pp. 12 454–12 470, Apr 2021. [Online]. Available: https://opg.optica.org/oe/abstract.cfm?URI=oe-29-8-12454

[29] J. M. Warnock and T. E. Van Zandt, "A statistical model to estimate the refractivity turbulence structure constant c^2n in the free atmosphere," 1985, technical Memorandum. [Online]. Available: https://repository.library.noaa.gov/view/noaa/23564

[30] G. Jumper, J. Roadcap, P. Tracy, E. Murphy, D. Mattes, and J. Myers, "T-rex: Afrl radiosonde and thermosonde data. version 1.0," 2007. [Online]. Available: https://data.eol.ucar.edu/dataset/92.048

[31] Wikipedia contributors, "Tropopause — Wikipedia, the free encyclopedia," 2021, [Online; accessed 3-December-2022]. [Online]. Available: https://en.wikipedia.org/w/index.php?title=Tropopause&oldid=1054120299

[32] D. Vanhoenacker-Janvier, C. Oestges, and A. Martellucci, "Prediction of scintillation cumulative statistics using classical and high resolution radiosoundings," in 2006 First European Conference on Antennas and Propagation, 2006, pp. 1–5.

[33] "Weather Research amp; Forecasting Model (WRF) | Mesoscale amp; Microscale Meteorology Laboratory — mmm.ucar.edu," https://www.mmm.ucar.edu/models/wrf, [Accessed 16-Dec-2022].

[34] "Copernicus Climate Data Store | — cds.climate.copernicus.eu," https://cds.climate.copernicus.eu/cdsapp#!/dataset/reanalysis-era5-single-levels?tab=overview, [Accessed 27-Dec-2022].

[35] "ERA5: data documentation - Copernicus Knowledge Base - ECMWF Confluence Wiki — confluence.ecmwf.int," https://confluence.ecmwf.int/display/CKB/ERA5%3A+data+documentation, [Accessed 27-Dec-2022].

[36] F. Quatresooz, G. Orban de Xivry, O. Absil, D. Vanhoenacker-Janvier, and C. Oestges, "Challenges for optical turbulence characterization and prediction at optical communication sites," 2022.

UNIVERSITÉ CATHOLIQUE DE LOUVAIN
École polytechnique de Louvain
Rue Archimède, 1 bte L6.11.01, 1348 Louvain-la-Neuve, Belgique | **www.uclouvain.be/epl**